

RESEARCH ARTICLE | MAY 01 2004

Heating and current drive by electron cyclotron waves

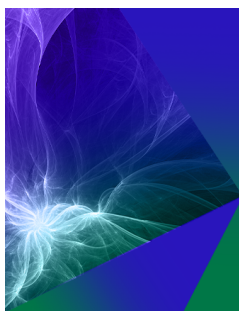
R. Prater



Phys. Plasmas 11, 2349–2376 (2004)

<https://doi.org/10.1063/1.1690762>






Physics of Plasmas

[Learn more](#)

Read our Author Testimonials

Physics of Plasmas has a
9.1 author satisfaction rating



Heating and current drive by electron cyclotron waves^{a)}

R. Prater^{b)}
General Atomics, San Diego, California 92186-5608

(Received 29 October 2003; accepted 5 February 2004; published online 23 April 2004)

The physics model of electron cyclotron heating (ECH) and current drive (ECCD) is becoming well validated through systematic comparisons of theory and experiment. This work has shown that ECH and ECCD can be highly localized and robustly controlled in toroidal plasma confinement systems, leading to applications including stabilization of magnetohydrodynamic instabilities like neoclassical tearing modes, control and sustainment of desired profiles of current density and plasma pressure, and studies of localized transport in laboratory plasmas. The experimental work was supported by a broad base of theory based on first principles which is now well encapsulated in linear ray tracing codes describing wave propagation, absorption, and current drive and in fully relativistic quasilinear Fokker–Planck codes describing in detail the response of the electrons to the energy transferred from the wave. The subtle balance between wave-induced diffusion and Coulomb relaxation in velocity space provides an understanding of the effects of trapping of current-carrying electrons in the magnetic well. Strong quasilinear effects and radial transport of electrons, which may broaden the driven current profile, have also been observed under some conditions and appear to be consistent with theory, but in large devices these are usually insignificant. The agreement of theory and experiment, the wide range of established applications, and the technical advantages of ECH support the application of ECH in next-step tokamaks and stellarators. © 2004 American Institute of Physics. [DOI: 10.1063/1.1690762]

TABLE OF CONTENTS

I. INTRODUCTION..... 2349

II. EC WAVE PHYSICS..... 2350

 A. Propagation and accessibility..... 2350

 B. Wave launching..... 2353

 C. Polarization..... 2353

 D. Ray trajectories..... 2354

 E. Wave/particle resonance..... 2354

 F. Wave absorption..... 2354

 G. Hot plasma effects..... 2356

 H. Resonance behavior..... 2357

 I. Experimental validation of wave propagation and absorption..... 2358

III. ELECTRON CYCLOTRON CURRENT DRIVE (ECCD)..... 2361

 A. Fisch–Boozer and Ohkawa current drive..... 2361

 B. Current drive efficiency..... 2362

 C. Interaction in velocity space..... 2364

 D. Techniques for measurement of ECCD..... 2366

 E. Comparison of ECCD with theory..... 2368

IV. APPLICATIONS OF ECH/ECCD..... 2371

V. SUMMARY..... 2373

I. INTRODUCTION

Electron cyclotron heating (ECH) and electron cyclotron current drive (ECCD) by means of electromagnetic waves in the frequency range of the electron cyclotron frequency and

its low harmonics has become a well established and widely used approach to heating plasmas and driving current in toroidal magnetic confinement devices for fusion energy applications. See, for example, the reviews^{1–8} and references therein. The characteristic ability of ECH and ECCD to deposit power or current in a highly localized, robustly controllable way makes these techniques applicable to many objectives not addressable by other heating or current drive approaches. ECH and ECCD have been applied to such objectives as plasma generation and global heating, the support and maintenance of desired current profiles in tokamaks and neutralization of the bootstrap current in stellarators, stabilization of magnetohydrodynamic (MHD) instabilities, and studies of plasma transport through localized heating. This body of work is supported by a confluence of theory, as encapsulated in practical computer codes, and the experimental validation of that theory over a wide range of plasma conditions. This provides a high degree of confidence in the projection of applications of electron cyclotron (EC) waves in future devices.

The use of EC waves has practical advantages as well. Chief among these is that the EC wave propagates in vacuum and couples efficiently to the plasma at its boundary, unlike other rf techniques. Furthermore, the wave may propagate as a narrow, well-defined beam. This means that the wave launcher may be distant from the plasma and that the coupling is insensitive to the conditions at the plasma boundary. These are important advantages for a thermonuclear device like the International Thermonuclear Experiment Reactor (ITER),⁹ where objects close to the plasma will be at risk of damage. Dynamic steering of the EC power can be done by using moving parts far removed from the vacuum vessel, as pointed out originally by Moeller and co-workers,¹⁰ eliminat-

^{a)}Paper JR1 1, Bull. Am. Phys. Soc. **48**, 167 (2003).
^{b)}Invited speaker.

ing the need for movable mirrors inside the vacuum vessel. In addition, the peak power density can be very high at the antenna, routinely reaching $3 \times 10^8 \text{ W/m}^2$ in present devices. High power density implies that the antennas can be small, with corresponding benefits regarding neutron shielding, containment of tritium, and mechanical support. Because of the short wavelengths involved, even small antennas have modest diffraction so that the beam of EC power stays narrow, supporting applications that need highly localized deposition.

Work with high power EC waves was made possible by the development of the gyrotron starting in the 1970s. The gyrotron is a source of high power in the frequency range corresponding to the electron cyclotron frequency in the plasma, typically 28 to 170 GHz for modern tokamaks or stellarators. For an excellent review of the state of the art of gyrotron development see Ref. 11. Early gyrotrons were limited in a combination of power, pulse length, and frequency by dissipation and cooling of the microwave window. The windows were made typically of a ceramic like boron nitride or beryllium oxide and cooled at the edge or of sapphire with surface cooling by low-loss fluids. The development of windows made of synthetic diamond (reviewed in Ref. 12) in the late 1990s took advantage of the low dissipation, excellent thermal conductivity (four times that of copper), and high mechanical strength of this material and opened the way for gyrotrons with long pulse power exceeding 1 MW in the frequency range needed for present devices and for ITER (110 to 170 GHz). Practical use of a “depressed collector” to recover some of the power in the spent electron beam by electrostatic deceleration has improved the electrical efficiency from 30% to above 50%.¹³ The power may be transmitted to the plasma with high efficiency,¹⁴ so the power source may be far from the plasma, providing flexibility in source placement.

This combination of factors—the predictive understanding of the physics, the experimental demonstration of applications of this physics, and the development of suitable high power sources—has generated a tremendous flowering of experimental results in recent years. Over the past several years EC systems in the MW range have been implemented on the Axisymmetric Divertor Experiment Upgrade (ASDEX Upgrade),¹⁵ Compact Assembly-D (COMPASS-D),¹⁶ DIII-D,¹⁷ Frascati Tokamak Upgrade (FTU),¹⁸ Japanese Atomic Energy Research Institute Tokamak-60 Upgrade (JT-60U),^{19,20} Tokamak-10 (T-10),²¹ Tokamak à Configuration Variable (TCV),²² Tokamak Experiment for Technology Oriented Research (TEXTOR),^{23,24} and Tore Supra²⁵ tokamaks and the Large Helical Device (LHD)²⁶ and Wendelstein 7-AS²⁷ stellarators. Major new implementations are planned for the next generation of devices, the Wendelstein 7-X stellarator^{27–29} and the ITER tokamak.^{9,30} Some parameters of these systems are shown in Table I.

In this paper the physics of ECH in toroidal magnetic systems is reviewed in Sec. II and the physics of ECCD in Sec. III. In each section some recent experiments in which the physics was specifically tested and compared to theory are presented. In Sec. IV brief descriptions are provided of some recent work in which the properties of ECH or ECCD

TABLE I. Toroidal devices with EC systems in the MW power range. All systems are either operating or in active construction, except for the ITER system which is planned. The powers specified are nominal source powers.

Device	Power (MW)	Frequency (GHz)	Mode
ASDEX Upgrade	2.0	140	X2
COMPASS-D	2.0	60	X1, O1, X2
DIII-D	5.0	110	X2
FTU	1.6	140	O1
JT-60U	4.0	110	O1, X2
T-10	1.6	140	X2
TCV	3.0	82.7	X2
	1.5	118	X3
TEXTOR	0.4	110	X2
	1.0	140	X2
TORE SUPRA	1.0	118	O1, X2
LHD	2.5	84	O1
	1.5	170	X2
Wendelstein 7-X	10.0	140	X2
ITER	20.0	170	O1

are applied to study or improve plasma performance. References cited are only for example, and completeness is not an objective; for a more complete discussion of applications see the reviews cited above.^{5,6,8}

II. EC WAVE PHYSICS

In order to use EC waves effectively it is necessary to have a quantitative model for how the wave may be launched at the plasma boundary, how it propagates in a plasma, and how it is absorbed. Many of the basic features of wave propagation and the maximum density at which the wave can exist can be understood from the cold plasma model, described in Sec. II A. The propagation limits place conditions on the launching of the waves at the plasma boundary, addressed in Sec. II B. The polarization of the wave strongly affects the absorption process, and this is treated in Sec. II C. Sec. II D describes the calculation of ray trajectories in the plasma. The wave-particle interaction near a cyclotron resonance is presented in Sec. II E. Sec. II F describes the absorption process. Absorption can be understood from a simple classical picture that includes finite Larmor radius effects for the cyclotron harmonics, although quantitative calculations require relativistic effects as described in Sec. II G. Relativistic effects are always important in determining the form of the cyclotron resonance in velocity space, as described in Sec. II H. The form of the resonance curve will be seen in Sec. III to strongly affect current drive. Many of the salient features of the propagation and absorption have been tested in experiments, which are described in Sec. III.

Propagation and accessibility

We are interested here in waves which are in the frequency range of the electron cyclotron resonance or its low harmonics. The electron cyclotron angular frequency Ω_e is given by $\Omega_e = |e|B/m_0$, where B is the magnetic field and m_0 is the electron rest mass, giving $f_{ce} = \Omega_e/2\pi = 28 \text{ GHz/T}$. Propagation of the EC wave can be adequately described in the cold plasma limit in many cases of interest

(see Sec. II G for exceptions). Summarizing the treatment presented by Stix³¹ here for completeness, in this limit the electrons and ions are zero-temperature frictionless charged fluids in a constant magnetic field. The dispersion relation can be written in the form

$$D\left(n, \frac{\omega_p^2}{\omega^2}, \frac{\Omega_e}{\omega}, \theta\right) = \tan^2 \theta + \frac{P(n^2 - R)(n^2 - L)}{(Sn^2 - RL)(n^2 - P)} = 0, \quad (1)$$

where $n = c|\vec{k}|/\omega$ is the index of refraction, ω is the frequency of the wave, $\omega_p = (n_e e^2 / \epsilon_0 m_e)^{1/2}$ is the electron plasma frequency, θ is the angle between the wave vector \vec{k} and the magnetic field \vec{B} , and in the limit that the ion mass is much greater than the electron mass,

$$\begin{aligned} P &= 1 - (\omega_p / \omega)^2, \\ R &= (P - \Omega_e / \omega) / (1 - \Omega_e / \omega), \\ L &= (P + \Omega_e / \omega) / (1 + \Omega_e / \omega), \end{aligned} \quad (2)$$

and $S = (R + L)/2$ and $D = (R - L)/2$. From Eq. (1) for $\theta = \pi/2$ (perpendicular propagation) the solutions are

$$n^2 = P \quad \text{and} \quad n^2 = \frac{RL}{S}, \quad (3)$$

which transform smoothly as $\theta \rightarrow 0$ (parallel propagation) into

$$n^2 = L \quad \text{and} \quad n^2 = R. \quad (4)$$

These two solutions to the dispersion relation form the normal modes of wave propagation in the plasma. The mode associated with $n^2 = P$ for perpendicular propagation and with $n^2 = L$ for parallel propagation is called the ordinary mode (O-mode) and the other mode is the extraordinary mode (X-mode).

The propagation limits of these modes are given by the cutoffs ($n^2 = 0$) and resonances ($n^2 \rightarrow \infty$). At the physical location of a cutoff the wave is reflected. The cutoffs can be easily seen by writing the dispersion relation in the alternate form³¹

$$An^4 + Bn^2 + PRL = 0, \quad (5)$$

where A and B are algebraic functions of P, R, L , and θ . From Eq. (5), cutoff takes place where the product PRL equals zero. These are shown in Fig. 1(a) for the O-mode in the customary Clemmow–Mullaly–Allis (CMA) diagram,³¹ in which the abscissa is ω_p^2 / ω^2 (proportional to electron density n_e) and the ordinate is Ω_e^2 / ω^2 (proportional to B^2). For the O-mode the cutoff is $P = 0$, which is dependent only on the density, $\omega_p^2 = \omega^2$. For $\omega = \ell \Omega_e$, where ℓ is the harmonic number, this cutoff density n_{co} is given by $n_{co}(10^{20} \text{ m}^{-3}) = \ell^2 B_T^2 / 10.3$, where B_T is the magnetic field in units of Tesla. Propagation from the outside of the plasma ($\omega_p^2 / \omega^2 = 0$) to the cyclotron resonance or its harmonics is possible from either the low-field side or the high-field side of the plasma to the cyclotron resonance provided the region with $\omega_p^2 \geq \omega^2$ is avoided. This is illustrated for schematic tokamak geometry in Fig. 1(b). In practice, wave refraction becomes important for waves with $\theta \neq \pi/2$ as the density approaches

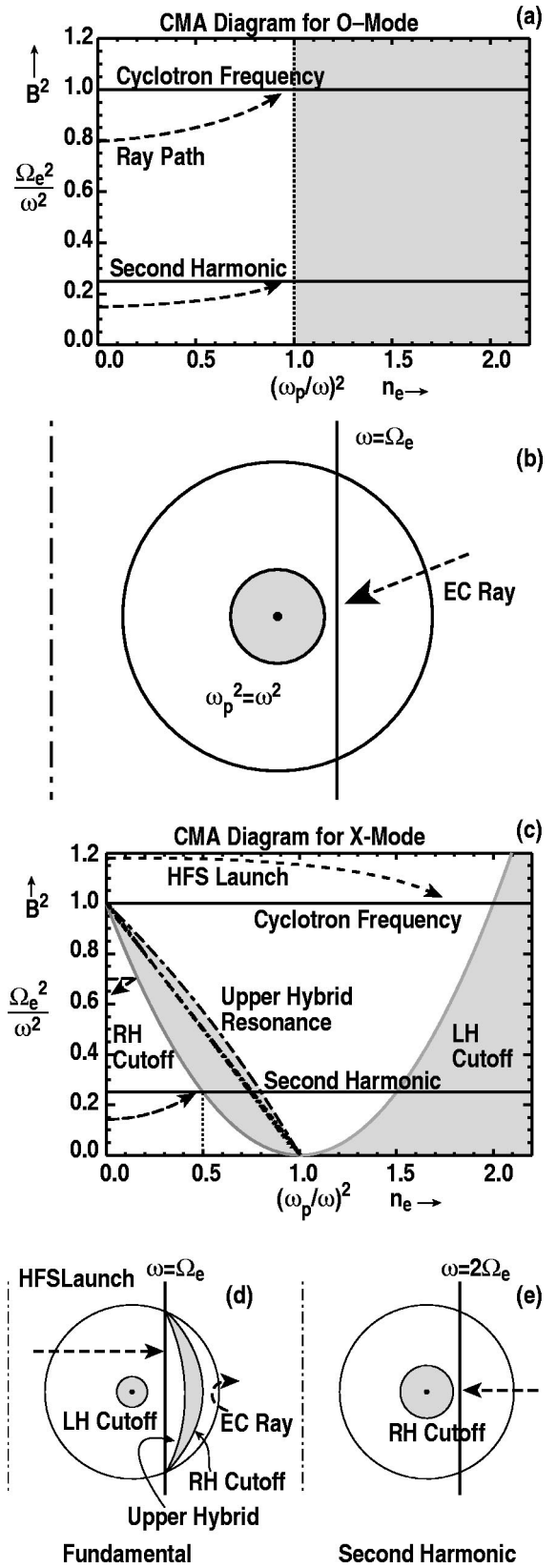


FIG. 1. (a) CMA diagram for the O-mode. (b) Typical ray trajectory for the O-mode in a schematic tokamak geometry in which the chain-dashed line represents the axis of symmetry and the magnetic field falls inversely with major radius. (c) CMA diagram for the X-mode showing the right-hand and left-hand cutoffs and the upper hybrid resonance for $\theta = 60$ deg (upper chain-dashed line) and 90 deg (lower chain-dashed line). (d) Typical ray trajectories for the fundamental and (e) for the second harmonic. In all cases the dashed arrows represent possible ray trajectories.

the cutoff density and propagation all the way to the cutoff may not be possible. It should be noted that where the wave frequency is near the cyclotron frequency or its harmonics there may be a single-particle resonance between the electron motion and the wave fields which can result in energy transfer between the wave and the electron as discussed in Sec. II E, but in the sense of the mode resonance described here ($n^2 \rightarrow \infty$) there are no resonances at the cyclotron frequency or its harmonics.

The behavior of the X-mode is more complicated. The X-mode experiences cutoff at $R=0$, the right-hand (RH) cutoff and $L=0$, the left-hand (LH) cutoff. The X-mode also has a resonance, the upper hybrid resonance, given by $\tan^2 \theta = P/S$ from Eq. (1) in the limit of very large n^2 . These cutoffs and resonance are shown in the CMA diagram for the X-mode in Fig. 1(c). The upper hybrid resonance depends on θ but only weakly for propagation not too far from perpendicular, the usual condition of interest for toroidal geometries. The shaded region between the RH cutoff and the upper hybrid resonance is a region of evanescence. The area in the X-mode CMA diagram below the cyclotron resonance and above the upper hybrid resonance and the LH cutoff represents a region of propagation of the wave, but in most cases of interest for fusion applications the wave cannot access this region since the only route into it crosses the fundamental resonance where absorption is usually strong.

The fundamental resonance is not accessible from the low field side because of the RH cutoff, so the waves must be launched from the high magnetic field side of the plasma as illustrated for a tokamak geometry in Fig. 1(d). This approach has the largest range of plasma density, up to twice the density limit of the fundamental O-mode (designated by the notation “O1-mode”). The factor 2 in the density limit can be seen in Fig. 1(c), where the cyclotron resonance intersects the LH cutoff at $\omega_p^2/\omega^2 = 2$. This approach suffers from the technical difficulty of launching the waves from the high field side, which means that the waves encounter the fundamental resonance in the transmission line in order to reach the launcher. It is possible but difficult to avoid breakdown in waveguide crossing the fundamental resonance. Two possible solutions are placing the microwave window also on the high field side, so that the waveguide is pressurized where it crosses the resonance so that the collision frequency of any free electron is much higher than the applied frequency, and splitting the waveguide and applying an electrical bias to sweep out any free electrons before secondary ionization can take place.³² Both methods seem problematic for a burning plasma experiment in a tokamak, but the pressurized waveguide may be acceptable for the high field side launch in some stellarator geometries.

The second harmonic X-mode (X2-mode) is accessible to densities up to half the cutoff density of the O-mode where $\omega_p^2 = \omega^2$, as shown in Fig. 1(c). If the second harmonic is achieved by doubling the frequency of the applied power, then the density limit for the X2-mode is double that of the O1-mode. Similarly, the X3-mode has still higher density limit. The behavior of the launch location and the density limits is shown in Table II for the modes of interest. The density limits for the X-mode may be written as $\omega_p^2 \leq 2\Omega_e^2$

TABLE II. Characteristics of the fundamental and low harmonic EC waves for propagation nearly perpendicular to the magnetic field. The magnetic field is fixed and harmonics are achieved by increasing the applied frequency. The density comparison is n_{01} , the density at which $\omega_p^2 = \Omega_e^2$. The density limits shown here are limits on propagation. The effects of refraction and the dependence of absorption on density may substantially reduce the limits in practice.

	O1	X1	X2	O2	X3
Frequency	Ω_e	Ω_e	$2\Omega_e$	$2\Omega_e$	$3\Omega_e$
Density	n_{01}	$2n_{01}$	$2n_{01}$	$4n_{01}$	$6n_{01}$

for $\ell=1$ and $\omega_p^2 \leq \ell(\ell-1)\Omega_e^2$ for $\ell \geq 2$, or $n_{co}(10^{20} \text{ m}^{-3}) = \ell(\ell-1)B_T^2/10.3$.

The cutoff density places constraints on the application of EC waves to plasmas. In tokamaks, for example, the operational density appears to be limited approximately by the Greenwald density,³³ $n_{GW} = I_{MA}/\pi a_m^2$, where n_{GW} is the limiting density in units of 10^{20} m^{-3} , a_m is the minor radius in units of m, and I_{MA} is the plasma current in units of MA. In Fig. 2 the ratio of the cutoff density for the fundamental O-mode to the Greenwald density is plotted as a function of the applied frequency for several example tokamaks using characteristic plasma currents and magnetic fields. For a high field tokamak like ITER the cutoff represents no limitation in the operating density. For intermediate field tokamaks like ASDEX Upgrade, DIII-D, and Tore Supra, the O1-mode represents an unacceptable limitation on the applicability of EC waves for many purposes. This is overcome in these devices by using the X2-mode, which has twice the cutoff density of the O1-mode. This raises the cutoff density to close to or greater than the Greenwald density. In TCV practical use of the X3-mode is being pioneered to access even higher density relative to the O1-mode cutoff.³⁴⁻³⁶ As will be discussed

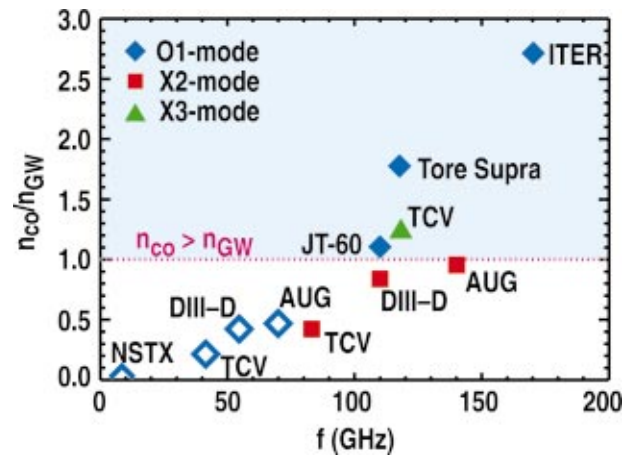


FIG. 2. (Color) The ratio of the fundamental O-mode cutoff density to the Greenwald density (diamonds) for some representative existing and projected tokamaks, as a function of the cyclotron frequency. Also shown are some cases in which the allowed operating density was increased by increasing the applied frequency and using the X2-mode (red squares) or X3-mode (green triangle). In calculating the Greenwald density, the toroidal field is assumed resonant at the plasma center, and the plasma current is 15 MA for ITER, 2.8 MA for JT-60U, 1.5 MA for Tore Supra, 1 MA for AUG, DIII-D, and NSTX, and 0.2 MA for TCV.

below, the dependence of the absorption on density may support effective heating by EC waves up to nearly the cutoff density, depending on the mode.

For devices with low magnetic field like the spherical torus NSTX, ECH is unusable due to the low upper limit on density.³⁷ However, for steep density gradients as in an H-mode edge the evanescent region between the RH cutoff and the upper hybrid resonance may be thin enough in space that tunneling can take place efficiently to the upper hybrid resonance where conversion to the electrostatic electron Bernstein wave (EBW) may take place. This is one approach, called the XB approach, to generation of electron Bernstein waves in the plasma interior. Another technique, called the OXB, avoids tunneling by using mode conversion from the O-mode to the X-mode with subsequent conversion to the EBW.³⁸ The EBW propagates without a density limit and is strongly damped near the cyclotron resonance. Both heating and current drive by means of EBWs have been achieved in the Wendelstein 7-AS stellarator³⁹ and in COMPASS-D.⁴⁰ For more on EBWs see the review by Laqua.⁴¹ The EBW will not be discussed further in this paper.

B. Wave launching

In the zero density limit of Eq. (1), the index of refraction is equal to unity for the X-mode and the O-mode; that is, the two modes in vacuum are degenerate electromagnetic waves propagating at the speed of light without attenuation from the launcher to the plasma. If the scale length for changes in the density at the plasma boundary is much longer than the wavelength and the density is low compared to the cutoff density (conditions commonly fulfilled), then the incident wave propagating in vacuum couples smoothly and without significant reflection to the modes inside the plasma. Once in the plasma the X-mode and O-mode propagate independently as normal modes of the plasma. The attractiveness of EC waves is in significant part a consequence of these coupling properties which imply that the launcher for the EC waves can be far from the plasma, unlike waves in the ion cyclotron or lower hybrid frequency ranges where an evanescent layer between the launcher and the plasma requires that the launcher lie very close to the plasma edge. For a burning plasma a remote launcher insensitive to the conditions of the plasma boundary has great advantages for system engineering.

The launcher for EC waves imposes the initial direction and polarization of the wave. The direction of the wave outside the plasma determines the starting geometry for wave propagation in the plasma. In practice the direction of the wave is typically determined by the launcher by simply projecting the wave coaxially from a terminated waveguide or reflecting such a wave from a mirror. It should be noted that any waveguide used at frequencies over about 30 GHz for high power must be over-moded (that is, $d \gg \lambda$, where λ is the free-space wavelength and d is the waveguide dimension) since the dissipation in fundamental mode waveguide would be overwhelming. The wavelength is in the range of 2 to 5 mm while the highly over-moded waveguides are typi-

cally of order 50 to 100 mm in diameter in recent and proposed high power installations.¹⁴ Because there is little difference in the phase speed of a wave in highly over-moded waveguide compared to vacuum, there is negligible reflection back down the waveguide where the waveguide ends. The over-moded waveguide carrying a low-order mode, typically the HE_{11} -mode in circular corrugated waveguide,¹⁴ produces a beam with divergence given roughly by the diffraction limit λ/d . For example, for 3 mm waves (100 GHz) the diffraction angle is 3° for 60 mm diameter waveguide. Steering mirrors are commonly used to change the angle of incidence on the plasma. The quantity Rk_ϕ is conserved in an axisymmetric configuration, where k_ϕ is the toroidal component of the wave vector, so in such a system the toroidal component of the wave propagation is controlled throughout the propagation of the ray by the launching angle. Mirrors may contain curvature to focus the beam to reduce its diameter at some location along its path.

C. Polarization

A second function of the launcher is to impose a polarization on the launched wave in order to couple it to the desired mode in the plasma. Once inside the plasma the wave propagates as a normal mode with the phase speed given by the dispersion relation, Eq. (1). The wave polarization at the plasma boundary determines which normal mode is excited, the X-mode or O-mode. Defining a local Cartesian coordinate system with the static magnetic field \vec{B} defining the z direction and \vec{k} in the x - z plane, the polarization of the normal modes is given by³¹

$$\frac{iE_y}{E_x} = \frac{D}{S - n^2}, \quad (6)$$

$$\frac{E_z}{E_x} = \frac{-n^2 \cos \theta \sin \theta}{P - n^2 \sin^2 \theta}, \quad (7)$$

where n denotes the index of refraction of either the X- or the O-mode. Since the right-hand side (RHS) of Eq. (6) is real, the x and y components of the wave electric field are 90° out of phase, so the polarization in the plane perpendicular to \vec{B} is in general elliptical with a principal axis (major or minor) along the y direction. For $iE_y/E_x < 0$, the ellipticity is right handed, which is the handedness of the electron gyromotion. As the wave propagates in a cold plasma the mode polarizations are maintained according to Eqs. (6) and (7), but mode purity may not be maintained perfectly if hot plasma effects are included;⁴² however, for parameters typical of fusion plasmas this remains a small effect.⁴²

In order to excite a single mode in the plasma, the polarization at the boundary is set to couple to the desired mode. The polarization at the plasma boundary is given by the low-density limit of Eq. (6). Rotated to a coordinate system in which \vec{k} is parallel to \hat{z} (that is, looking along the \vec{k} vector, which is the conventional way to describe wave polarization) the polarization is

$$\frac{iE_p}{E_y} = \frac{\Omega_e}{\omega} \left\{ \frac{\pm [\sin^4 \theta + 4 \cos^2 \theta / (\Omega_e / \omega)^2]^{1/2} - \sin^2 \theta}{2 \cos \theta} \right\}, \quad (8)$$

with the upper sign corresponding to the X-mode and the lower sign the O-mode.⁴³ Here E_p is the electric field in the plane containing \vec{k} and \vec{B} . For perpendicular propagation at the plasma edge the wave polarizations are linear. For oblique launch the polarizations given by Eq. (8) are elliptical. In practice, elliptical polarizations are generated by birefringent elements, usually rotatable grooved mirrors, in the miter bends of the transmission line.⁴⁴ For perfect coupling to a single mode, the ellipticity of the incident wave must be as given by Eq. (8), which is a function of the magnitude of the magnetic field and the angle of incidence in the local coordinate system described above, while the inclination of the ellipse must follow the y axis of that coordinate system which is a function of the magnetic pitch angle at the plasma boundary. As a mode propagates it may in practice experience conversion to the other mode.⁴⁵ Hot plasma effects can be particularly effective in causing mode conversion on the order of 10% to 20% when the resonance is in a region of large gradient in electron temperature, but this may in principle be corrected through modifications of the condition Eq. (8) if ray tracing including the hot plasma effects is performed.⁴² The mode conversion process due to magnetic shear has been evaluated for the LHD stellarator⁴⁶ and found to be qualitatively in agreement with experiment.⁴⁷

D. Ray trajectories

The CMA diagram indicates the limits on wave propagation, but it provides no information regarding the actual trajectory of waves in the plasma. To provide this information, ray tracing codes or Gaussian beam propagation codes are used. The ray tracing codes assume geometric optics: that is, a Gaussian beam may under some conditions be simulated as an array of independently propagating rays. The rays are oriented around a central ray which describes the direction of the beam. Typically the equally weighted rays are arranged to simulate the far-field power profile of a Gaussian beam. The propagation of each independent ray in the inhomogeneous anisotropic medium of a plasma in a magnetic field (that is, with arbitrarily varying dielectric tensor) is described by the equations⁴⁸

$$\frac{d\vec{r}}{dt} = -\frac{\partial D / \partial \vec{k}}{\partial D / \partial \omega}, \quad \frac{d\vec{k}}{dt} = \frac{\partial D / \partial \vec{r}}{\partial D / \partial \omega}, \quad (9)$$

where D is the real part of the dispersion relation [equivalent to Eqs. (1) or (5)] and \vec{r} is the spatial location along the ray. These equations are integrated to find the ray trajectory and the wave number along that trajectory. Ray tracing codes like TORAY-GA^{49,50} and BANDIT-3D⁵¹ use this approach.

In cases in which the beam is converging due to a focusing element and the beam spread is not large, the geometric optics of ray tracing is inaccurate and the beam propagation approach may be required. In this approach the trajectory of the center of the beam is determined as in the ray tracing case, but the transverse properties of the wave like the cur-

vature of the phase front and the radial attenuation of the wave fields are determined in a way which naturally includes the diffraction and self-interference effects. Gaussian beam codes include TORBEAM⁵² and ECWGB.^{53,54}

E. Wave/particle resonance

Electron cyclotron waves may be absorbed by cyclotron damping near the cyclotron resonance or its harmonics. The Doppler-shifted relativistic resonance condition at the ℓ 'th harmonic is satisfied by electrons which have velocity components satisfying

$$\omega = \frac{\ell \Omega_e}{\gamma} + k_{\parallel} v_{\parallel}, \quad (10)$$

where $\gamma = (1 - v_{\perp}^2/c^2 - v_{\parallel}^2/c^2)^{-1/2}$ is the usual relativistic factor, v_{\parallel} and v_{\perp} are the components of the velocity parallel and perpendicular to the magnetic field, and $k_{\parallel} = \omega n_{\parallel}/c$ is the component of \vec{k} parallel to \vec{B} . Even for plasmas satisfying the condition $kT_e \ll mc^2$ the relativistic downshift of the resonance frequency is important. Equation (10) can be written fully relativistically as

$$\frac{v_{\perp}^2}{v_t^2} = \left(1 - \frac{\omega^2}{\ell^2 \Omega_e^2} \right) \frac{c^2}{v_t^2} + 2n_{\parallel} \frac{\omega^2}{\ell^2 \Omega_e^2} \frac{c}{v_t} \frac{v_{\parallel}}{v_t} - \left(1 + n_{\parallel}^2 \frac{\omega^2}{\ell^2 \Omega_e^2} \right) \frac{v_{\parallel}^2}{v_t^2}, \quad (11)$$

where $T_* = kT_e/mc^2$ and v_t is the relativistic analog of the thermal velocity given by $v_t = c \sqrt{(2T_* + T_*^2)/(1 + 2T_* + T_*^2)}$, which reduces to $mv_t^2/2 = kT_e$ in the limit of small T_e . Equation (11) describes an ellipse in velocity space (v_{\perp}, v_{\parallel}) with both foci on the $v_{\perp} = 0$ axis. For $n_{\parallel} = 0$ the resonance ellipse degenerates into a circle centered on the origin since the relativistic frequency shift depends only on $(v/c)^2$. The RHS of Eq. (11) is negative on the low field side of the resonance when $n_{\parallel}^2 \leq 1 - \ell^2 \Omega_e^2 / \omega^2$. For this condition there are no resonant electrons since for that n_{\parallel} and magnetic field the parallel velocity required to achieve the necessary Doppler upshift in frequency generates a larger offsetting relativistic downshift in frequency due to the mass increase, so that the resonance condition cannot be achieved at any velocity. This is described as the “pinch point” in Ref. 55. Parallel Landau damping does not take place for EC waves because the parallel phase velocity c/n_{\parallel} is greater than or equal to the speed of light, so there can be no resonant electrons.

F. Wave absorption

Many features of the basic cyclotron interaction can be understood by considering the wave/particle interaction at the simplest level.^{31,56} The nonrelativistic equation of motion for an electron with nonzero energy in a magnetic field in the z direction and a plane wave with wave number k_{\perp} in the x - z plane is

$$m d\vec{v}/dt = q(\vec{E} + \vec{v} \times \vec{B}), \quad (12)$$

where \vec{E} is the wave electric field and \vec{B} is the static background field. It is assumed that the wave field is small enough that the particle orbits are nearly unperturbed by the interaction with the wave. The forces due to $\vec{v} \times \vec{B}_w$, where \vec{B}_w is the wave magnetic field, may affect the direction of the motion but being normal to the velocity they cannot change the energy of the electron. The components of Eq. (12) may be written

$$\dot{v}_x + \Omega_e v_y = -(e/m)E_x \cos(k_\perp x - \omega t),$$

$$\dot{v}_y - \Omega_e v_x = -(e/m)E_y \sin(k_\perp x - \omega t),$$

$$\dot{v}_\parallel = -(e/m)E_\parallel \cos(k_\perp x - \omega t).$$

Knowing that electrons have right-handed orbits about the magnetic field, we define the right-hand components $v_- = v_x - i v_y$ and $E_- = E_x - i E_y$. Then using $x = \rho_e \sin \Omega_e t$ to reflect the gyromotion of the electron, where $\rho_e = m v_\perp / e B$ is the Larmor radius, and applying power at the ℓ 'th harmonic $\omega = \ell \Omega_e$, Eq. (12) becomes

$$\dot{v}_- + i \Omega_e v_- = -(e/m)E_- \exp[-i(k_\perp \rho_e \sin \Omega_e t - \ell \Omega_e t)]$$

and

$$\dot{v}_\parallel = -(e/m)E_\parallel \exp(-i k_\perp \rho_e \sin \Omega_e t),$$

neglecting the effect of the nonresonant E_+ term. Applying the Bessel function identity

$$\exp[i \xi \sin \varphi] = \sum_{p=-\infty}^{\infty} \exp(ip\varphi) J_p(\xi)$$

with $\xi = k_\perp \rho_e$ and $\varphi = \Omega_e t$ to expand the plane wave in terms of cylindrical waves, and under the quasilinear approximation that the electron orbit is weakly perturbed by the interaction with the wave fields, the equations of motion become

$$\dot{v}_- + i \Omega_e v_- = -\frac{e E_-}{m} \sum_p J_p(k_\perp \rho_e) \exp[i(p - \ell) \Omega_e t], \quad (13)$$

$$\dot{v}_\parallel = -\frac{e E_\parallel}{m} \sum_p J_p(k_\perp \rho_e) \exp(ip \Omega_e t). \quad (14)$$

Net time-averaged absorption occurs most strongly for the term in the expansion which matches the time behavior of the left-hand side (LHS). The time behavior of the LHS of Eq. (13) is $\exp(-i \Omega_e t)$ for the perpendicular motion driven by the E_- component. This is matched for the term $p = \ell - 1$. For the parallel motion the $p = \ell$ term provides time-averaged acceleration, one order higher in the Bessel function. Then we can write the change in the energy $\delta W = (m \vec{v} \cdot d\vec{v}/dt) \tau_c$, where τ_c is the time over which the electron and the wave stay correlated in phase, to the lowest order in the Bessel function expansion as

$$\delta W_\perp = -e v_- E_- J_{\ell-1}(k_\perp \rho_e) \tau_c, \quad (15)$$

$$\delta W_\parallel = -e v_\parallel E_\parallel J_\ell(k_\perp \rho_e) \tau_c.$$

The energy changes of Eq. (15) are dependent on the phase of the gyromotion relative to that of the wave, and some electrons will gain energy from the wave while others

will lose energy. The assumption is made that when an electron re-enters the EC beam it has lost its correlation in gyrophase with the wave through an irreversible process like collisions. Averaging over an ensemble of electrons with random gyrophase, the increase in energy of the distribution is a diffusion process in velocity for which the step size in energy is given by Eq. (15). Evaluation of the heating process described by Eq. (15) for an ensemble of random phase and performing a time average results in an diffusion coefficient, again to lowest order in the Bessel function expansion, for resonant electrons proportional to the factor⁵⁶

$$G_\ell = |v_\perp E_- J_{\ell-1}(k_\perp \rho_e) + v_\parallel E_\parallel J_\ell(k_\perp \rho_e)|^2. \quad (16)$$

Some of the key features of electron cyclotron heating may be deduced from this simple treatment. First, for a cold plasma only the fundamental has absorption. The argument of the Bessel function can be written as $k_\perp \rho_e = n_\perp \ell v_t / c = n_\perp \ell \sqrt{T_e / mc^2}$ for a thermal electron. Since n_\perp and ℓ are of order unity, this implies that $k_\perp \rho_e$ is small for low harmonics even in high temperature plasmas. For small argument the Bessel function can be expanded as $J_{\ell-1}(k_\perp \rho_e) \propto (k_\perp \rho_e)^{\ell-1}$ so only the fundamental ($\ell = 1$) has absorption if $T_e \approx 0$. Second, the heating depends on the right-hand component of the electric field E_- and more weakly (that is, to one higher order in the Bessel function) on the parallel field E_\parallel . Third, from Eq. (16) the interaction at succeeding harmonics for any given electric field polarization decreases roughly by the small factor $(k_\perp \rho_e)^2 \approx T_e / mc^2$. It will be shown later that the dependence of absorption on $k_\perp \rho$ is important for effective electron cyclotron current drive.

One might think that the fundamental O-mode would have strong absorption even for $k_\perp \rho = 0$ since the first term of Eq. (16) is proportional to $J_0(k_\perp \rho_e) \approx 1$. However, for the O-mode the component of the electric field with right-hand helicity, E_- , is zero in the cold plasma approximation. This is illustrated in Fig. 3(a), which shows the fractional wave power in the RH, LH, and parallel polarizations as a function of the normalized density, ω_p^2 / ω^2 , for several angles between \vec{B} and \vec{k} . For all angles of propagation, the RH component is absent. Hence the absorption is proportional to $E_\parallel^2 J_1^2(k_\perp \rho_e) \propto E_\parallel^2 T_e$. The wave absorption is also an increasing function of density due in part to the evolution of the polarization from LH to parallel polarization as the density increases, as shown in Fig. 3(a). For the X2-mode the polarization is shown in Fig. 3(b), which indicates that the wave starts at 50% or higher RH polarized and becomes even more RH polarized as the density increases. Hence the wave absorption is very similar in behavior and magnitude to that of the fundamental O-mode.

The fundamental X-mode is a more complicated case. The polarizations shown in Fig. 3(c) show that the RH component is large at very low density, but it changes to parallel polarization for moderate densities and to pure LH near the maximum density. For low densities with $\omega_p^2 / \omega^2 \leq 0.1$ this mode is strongly absorbed even at zero T_e ; that is, finite Larmor radius effects are not needed. This behavior makes the fundamental X-mode ideal for generating breakdown of a

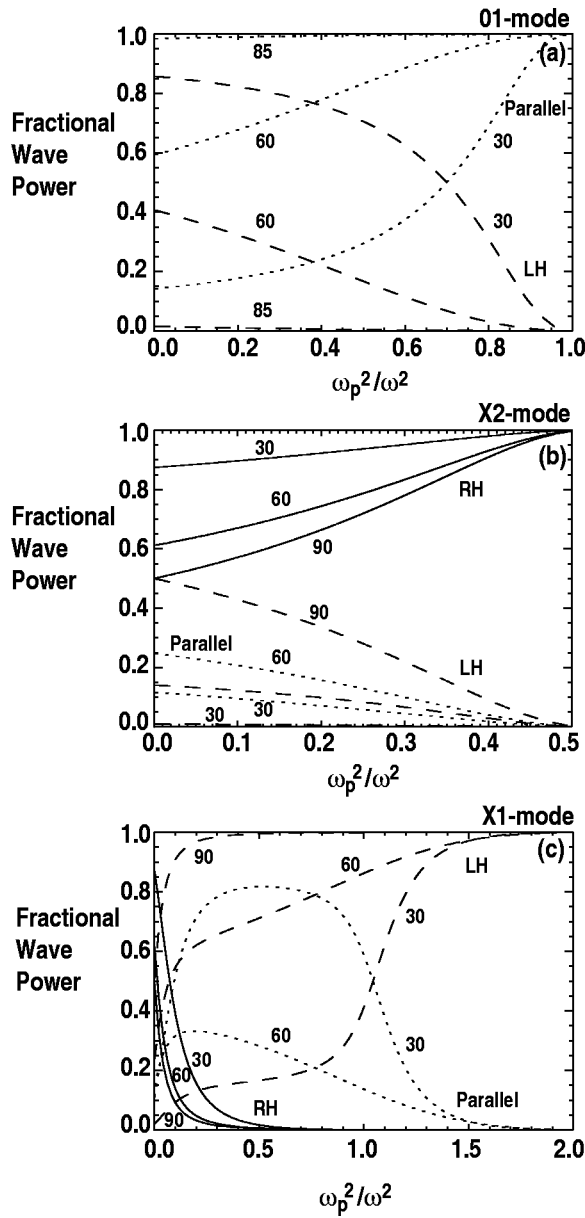


FIG. 3. Fractional wave power in the polarization determined from the cold plasma dispersion relation for (a) the O1-mode, (b) the X2-mode, and (c) the X1-mode, as a function of the normalized density ω_p^2/ω^2 . The solid lines represent the polarization with right-hand (RH) helicity, the dashed lines with left-hand (LH) helicity, and the dotted lines are for the wave electric field polarized along the magnetic field direction (parallel). The parameters indicated are the angle (in degrees) between the wave vector and the magnetic field. The quantity Ω_e/ω is 0.95 for (a), 0.48 for (b), and 1.05 for (c).

gas in a magnetic trap. For higher densities nonzero T_e is required and the absorption is approximately inversely proportional to density.

G. Hot plasma effects

While much can be learned about the general behavior of wave propagation and absorption from the simple treatment given in the preceding section, hot plasma effects are important and must be included in a self-consistent way. A large body of theoretical work was carried out in the 1980s to do this; see particularly the summary by Bornatici¹ and the

references therein. A frequently used calculational procedure is given by Fidone⁵⁷ and extended to higher harmonics by Mazzucato *et al.*⁵⁸ The elements of the cold plasma dispersion tensor from which Eq. (1) is derived are modified at finite temperature by addition of terms dependent on T_e and proportional to density (i.e., ω_p^2/ω^2) due to the hot plasma dielectric, plus anti-Hermitian parts which are expanded in powers of $k_\perp \rho_e$. The usual Wentzel-Kramers-Brillouin¹ formulation of ray tracing requires that the anti-Hermitian part of the dielectric tensor be small compared to the Hermitian part; that is, that the imaginary part of the wave number be small compared to the real part. This condition may be violated near the cyclotron harmonics, however.⁵⁹ In cases where the wave is propagating nearly parallel to the resonance, as in top launch in a tokamak, the hot plasma modifications to the Hermitian part and the additions to the anti-Hermitian part may become comparable in magnitude to the Hermitian part. These hot plasma effects combine to make ray tracing and wave absorption inseparable processes. Relativistic effects are important even when the usual requirement $n_\parallel^2 \gg T_e/m_e c^2$ (i.e., that the parallel phase velocity is much smaller than the thermal velocity) is satisfied, and relativistic effects must be included unless the more restrictive condition $n_\parallel^2 \gg |1 - \Omega_e^2/\omega^2|$ is satisfied.⁵⁷ For heating and current drive in plasmas of fusion relevance this condition is so restrictive that relativistic calculations of absorption must always be used, and in some cases the calculation of the ray trajectories must use the hot plasma corrections as well.⁵⁹

The wave absorption can be expressed in terms of the optical depth $\tau = 2 \int \text{Im}(k) ds$ where the integral is along the ray path s . For the commonly used O1- and X2-modes including the hot plasma effects,

$$\begin{aligned} \tau_{\text{O1,X2}} &= \pi^2 n_{\text{O,X}} \frac{\omega_p^2}{\Omega_e^2} \frac{v_i^2}{c^2} \frac{L_B}{\lambda} f(\theta) g(\omega_p^2/\Omega_e^2) \\ &= \pi^2 n_{\text{O,X}} \frac{n_e}{n_{\text{O1}}} \frac{T_{\text{keV}}}{511} \frac{L_B}{\lambda} f(\theta) g(\omega_p^2/\Omega_e^2), \end{aligned} \quad (17)$$

where $L_B = B/(\partial B/\partial s)$ is the characteristic length along the ray over which the magnitude of the magnetic field changes and λ is the free-space wavelength,¹ and where the optical depth for the X2-mode is evaluated for quasiperpendicular propagation such that $\sin^4 \theta \gg 16 \cos^2 \theta$, or $80 < \theta < 100$ deg. For the O1-mode $g = 1$ and $f(\theta) = (1 + 2 \cos^2 \theta) \sin^4 \theta / (1 + \cos^2 \theta)^3 \approx \sin^3 \theta$. For the X2-mode $g = [(6 - \omega_p^2/\Omega_e^2)/(6 - 2\omega_p^2/\Omega_e^2)]^2$, an increasing function of density with values between 1 and 4, and $f(\theta) = \sin^2 \theta (1 + \cos^2 \theta)$. Equation (17) shows the close relationship between the magnitude and dependences of absorption of the O1- and the X2-modes. For most conditions of interest for fusion plasmas the optical depth is large for both the O1- and X2-modes. For the O2- and X3-modes the optical depth is smaller roughly by a factor T_e/mc^2 . In present day experiments the optical depth for these modes is typically smaller than unity, but in burning plasmas significant power may be absorbed by these modes with possible undesired effects.

H. Resonance behavior

The cyclotron resonance is strongly affected by relativistic effects even at quite low electron temperatures, as described in Sec. II E. This implies that calculations involving the resonance must be done fully relativistically and that the results are described most naturally in terms of momenta p_{\parallel} , p_{\perp} rather than the velocities v_{\parallel} , v_{\perp} . In this paper for heuristic purposes the results calculated relativistically may be presented in terms of velocities normalized by the thermal velocity v_t as a means of connecting more easily with the conventional physical intuition for the implications of a wave velocity of, say, three times v_t . This is an acceptable approximation for plasmas with temperature of a few keV or below, but of course it cannot be used for temperatures characteristic of a burning plasma where $3 v_t$ may be comparable to the speed of light.

The behavior of the resonance [Eq. (10)] along a ray strongly affects the physics of the wave-particle interaction. Consider, for example, a ray trajectory for the X2-mode calculated by the TORAY-GA ray tracing code in a tokamak geometry launched from above the midplane, as shown in Fig. 4(a). The ray travels with a path determined by applying Eq. (9) and uses a toroidal component in the launching angles such that $n_{\parallel} \approx 0.38$ near the intersection of the ray with the second harmonic resonance. At each step along the ray the local quantities B , T_e , and n_{\parallel} are known, so the resonance curve described by Eq. (11) is known. The resonance curves plotted in Fig. 4(b) correspond to the indicated points along the ray in Fig. 4(a). Also shown in Fig. 4(b) are the contours of constant density in velocity space and the local magnetic trapping boundary given by $v_{\perp}/v_{\parallel} = \sin^{-1}(\sqrt{B/B_{\max}})$, where B_{\max} is the maximum magnetic field on the flux surface, such that electrons with larger v_{\perp}/v_{\parallel} are trapped in the magnetic field well.⁶⁰ At the furthest point away from the resonance shown, the electron with smallest velocity which satisfies the resonance condition is near $2.5 v_t$. Since this is fairly far out in the distribution, there are few such electrons and the damping is weak. (From the discussion in Sec. II F absorption of this mode requires finite v_{\perp} , which moves the possible interaction along the resonance curve to even larger v_{\parallel} .) This can be also seen from Fig. 4(c), which shows that the imaginary part of the wave number k_i at this position along the ray is small, but rising rapidly. The power normalized to the incident power is decremented by 1% at this point. As the ray progresses further the frequency becomes closer to the resonant frequency as shown by the curve representing $2\Omega_e/\omega - 1$, so the resonance sinks deeper into the distribution since smaller v_{\parallel} is needed to obtain resonance. The absorption coefficient gradually rises and the normalized power remaining in the ray decreases. For the conditions of Fig. 4 the maximum rate of power loss, which is a balance between the increasing absorption rate k_i and the decreasing power remaining in the ray (i.e., not determined by the maximum of the absorption coefficient), occurs near the 50% power decrement. For the conditions of Fig. 4, then, the maximum rate of power decrement takes place when the minimum resonant v_{\parallel} is near v_t .

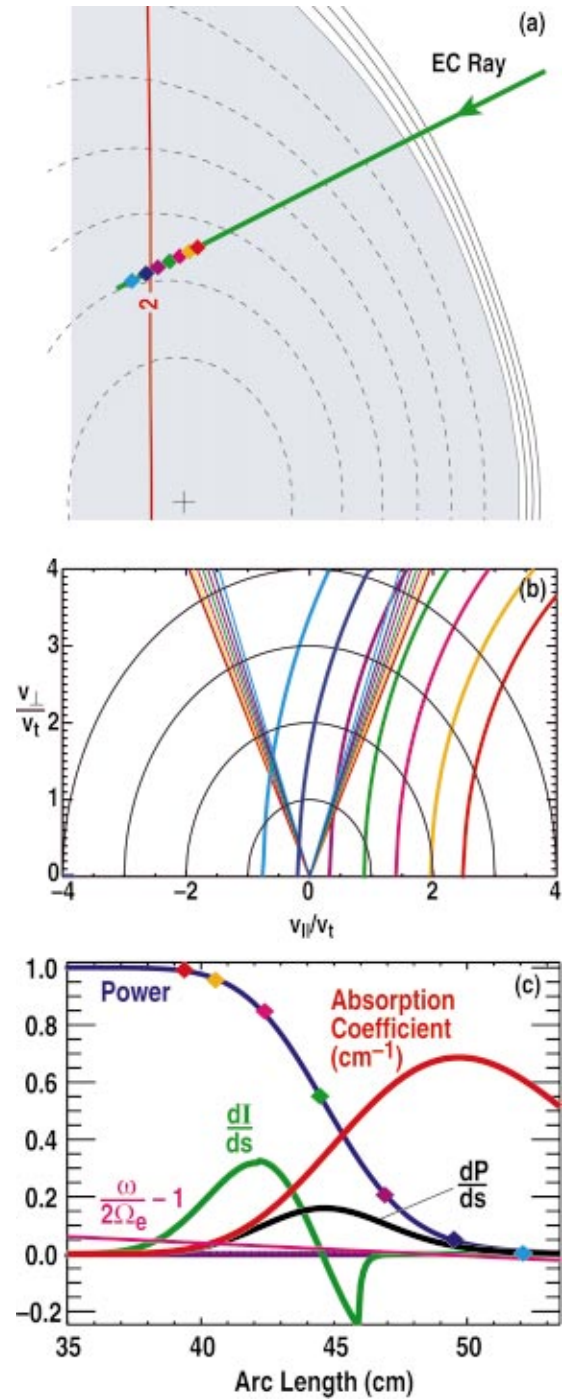


FIG. 4. (Color) (a) Example trajectory of a ray in tokamak geometry, as calculated by the TORAY-GA code for a discharge from DIII-D. The X2-mode is used with frequency 110 GHz, and the ray is launched such that the parallel index of refraction is 0.38 near the second harmonic resonance, shown as the vertical red line. The dashed lines are flux surfaces in the plasma. The local electron temperature is 1.43 keV and the density is $1.21 \times 10^{19} \text{ m}^{-3}$ at the location of the peak rate of absorption of the ray. (b) Resonance curves (colored curved lines) in velocity space, trapped particle boundary (colored straight lines), and contours of constant velocity (black curves). (c) Power in the ray normalized to the incident power, the power deposition rate $(1/P)(dP/ds)$ (cm^{-1}), the absorption coefficient (cm^{-1}), the quantity $\omega/2\Omega_e - 1$, and the deposition rate for electron cyclotron driven current dI/ds (200 A/cm/MW), as functions of length along the ray. The symbols in (a) and (c) and the curves in (b) have corresponding colors and are placed at absorbed powers of 1%, 5%, 20%, 50%, 80%, 95%, and 99% of the incident power.

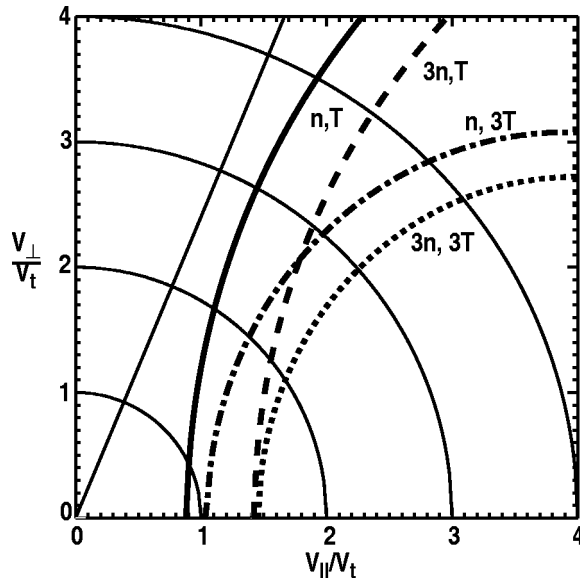


FIG. 5. Resonance curves in velocity space. The curve designated “ n,T ” is the resonance curve at the location of maximum power deposition from Fig. 4, for that low field side launch geometry. The other curves are for three times higher density (dashed), three times higher temperature (chain dash) and both three times higher density and temperature (dotted). For the last three curves the toroidal field and the ray launching angles are modified slightly to obtain the peak in absorption at the same location in physical space and same local value of $n_{||}=0.38$.

The expected heating profile in a plasma can be determined only by performing the ray tracing calculation. The local power deposition rate is determined by the absorption coefficient, the fraction of the power damped earlier along the ray, the trajectory and $n_{||}$ spread of the rays, and the geometry of how the rays cross flux surfaces and approach the resonance, as illustrated in Fig. 4. Under many circumstances the width of the power deposition profile is very small compared with the minor radius of the plasma.

Much of the physics of the EC wave/particle interaction is determined by where the resonance curve lies in velocity space. The resonance curve is a function of B and $n_{||}$, which vary along the ray. In order to describe how the curves shift with different parameters like density or temperature it is necessary to specialize to a particular point along the ray.⁶¹ In this discussion we use the point along the ray of maximum rate of absorption; i.e., the peak of the curve $(1/P)(dP/ds)$ of Fig. 4(c). (This point is near the 50% power decrement point if the ray is fully absorbed in the plasma.) In Fig. 5 the resonance curves for several conditions are plotted. These curves are obtained by running the ray tracing code in an iterative manner, adjusting the launching angles slightly and making small changes in the toroidal magnetic field such that the point of maximum rate of absorption occurs at the same location in physical space and with the same $n_{||}$. In this way the geometry and plasma parameters can be kept constant.^{61,62}

The behavior of the resonance with different density and temperature is illustrated in Fig. 5. The leftmost curve in this figure is the same as the resonance curve for 50% power decrement in Fig. 4(b). If the density is increased by a factor of 3 keeping the profile fixed, the curve obtained through the

process described above moves toward higher $v_{||}$. If instead the density is kept constant and T_e is increased by a factor of 3, the effect on the curve is primarily stronger curvature toward higher $v_{||}$. If both T_e and the density are increased, the curve moves strongly toward larger $v_{||}$ and stronger curvature. As a shorthand, it can be said that the resonance curve moves away from the trapping boundary when the product of density and temperature is increased, so the local quantity $\beta_e = n_e k T_e / (B^2 / 2\mu_0)$ is a useful way of characterizing the behavior of the resonance. Nevertheless, the middle two curves of Fig. 5 have the same β_e yet different form. The location of the resonance relative to the trapping boundary will be seen to have a very important effect on current drive by EC waves.

I. Experimental validation of wave propagation and absorption

The literature contains a very large body of work in which EC waves are used to heat a plasma (see references cited in Refs. 4–8). This work taken as a whole is supportive of the description of wave propagation limits and absorption characteristics described above. In many applications the intent of the experiment was simply to provide heating, but some experiments were designed to test the propagation limits in a systematic way. This turns out to be not so easy due to the ability of EC waves to reflect without much loss from the vessel walls, creating a cavity in which the plasma in the vicinity of the resonance is the lossiest element. In some cases, conversion between X-mode and O-mode at the walls due to reversal of the handedness of the polarization at a reflection can play an important role in the overall heating effectiveness for a mode which would be cut off otherwise.⁶³ Measurement of the profile of the heating is therefore more telling than the heating efficiency. The effect of the heating on energy and particle confinement can also complicate the response of the plasma to the EC heating profile.

For these reasons, experiments to test the propagation limits must be carefully designed. One way to directly test the propagation and absorption is to modulate the EC power and observe the transient plasma response, usually using measurements of electron cyclotron emission (ECE) at a series of closely spaced locations to determine the local electron temperature. Modulation may be a single step, in which the minimum delay of the ECE response at different minor radii may be used to determine the radius where the heating is taking place, or as a series of pulses for which Fourier analysis of the ECE channels can be performed (see Ref. 64 for a comparison of these techniques). Analysis of the radial behavior of the amplitude and phase of the response provides a sensitive measurement of the radial location of the heating. Experiments done this way have been able to distinguish directly between the propagation of the X-mode and O-mode at the second harmonic in DIII-D, which were found to be consistent with the ray tracing theory.^{65,66}

The modulated ECH approach has been very useful in validating the basic propagation and absorption model. Experiments on ASDEX Upgrade, for example, show excellent agreement of the width and location of the plasma response.

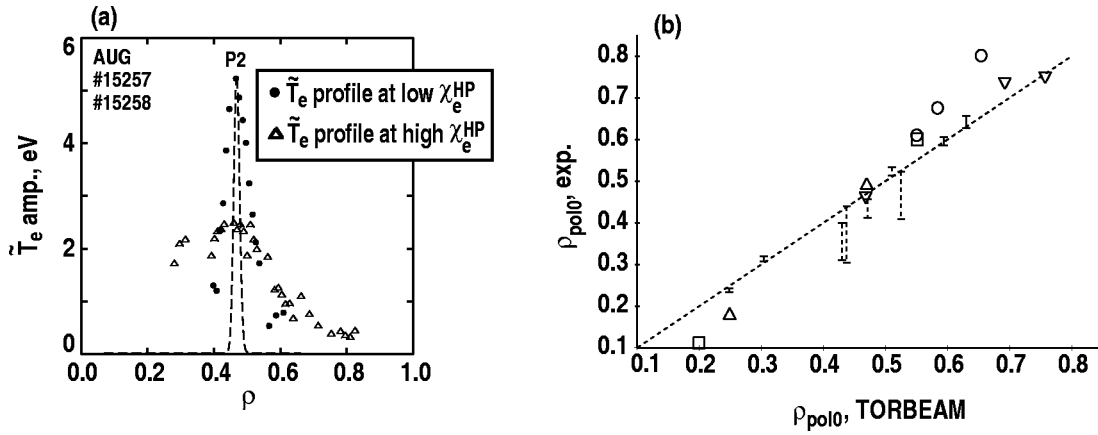


FIG. 6. (a) Fourier amplitude of the ECE measurements of T_e for ECH modulated at 500 Hz, as a function of normalized minor radius, for high and low diffusivity cases in ASDEX Upgrade. The high diffusivity is obtained by increasing the temperature gradient by applying ECH near the axis, while the low diffusivity case has ECH near $\rho=0.5$ in order to reduce the gradient. (b) Normalized minor radius ρ_{pol0} of the peak plasma response vs the theoretical value from TORBEAM calculations. The data points represented by solid lines are found from the break-in-slope technique at the initiation of the ECH pulse while the dashed lines are from the end of the pulse. The symbols are for the modulated ECH technique for different values of the magnetic field and the toroidal launch angle. Reprinted from Ref. 64.

The Fourier transform amplitudes can be plotted as a function of normalized minor radius for comparison with the code calculations as in Fig. 6(a). This figure⁶⁴ shows results for modulated ECH at $\rho=0.45$ for two values of the plasma diffusivity. In the low diffusivity case the plasma response is close to the calculated power profile (which is extremely narrow), while in the high diffusivity case the response is much broader, but both are clearly peaked at the expected value of ρ . The modulated ECH technique and the use of the break in slope of the T_e measurements both agree well with TORBEAM calculations in predicting the minor radius of the heating,⁶⁴ up to a normalized minor radius of 0.8, as shown in Fig. 6(b). Some similar measurements have been done on the L-2M stellarator.⁶⁷

Direct comparison of the theoretical absorption profile with the measured absorption profile in modern toroidal confinement devices is complicated by the effects of transport in broadening the profile of the ECE response, as shown in Fig. 6(a). The transport effects become relatively weaker as the

modulation frequency is raised, but the signal amplitude also becomes smaller. Recent work on ASDEX Upgrade⁶⁸ has shown that by using a range of modulation frequencies extending nearly to 1 kHz, the width of the deposition profile may be determined by fitting the amplitude and phase at the radial location of minimum phase delay with a slab model for the response including the effects of diffusion and damping. Typical data are shown in Fig. 7. For this low diffusivity case the inferred deposition profile is 23.5 ± 2.3 mm where the TORBEAM code calculates 10 mm.

Measurement of the integrated absorption can be made using detectors of wave power placed across the plasma from the antenna. Direct measurements of low power transmission of the X3-mode in Tore Supra⁶⁹ showed agreement with theory. This type of measurement has also been used to measure power absorption in the MTX tokamak,⁷⁰ in which a free electron laser was used to generate 20 ns pulses with extremely high power, up to 1 GW, launched from the low field side in the O1-mode. Data from such measurements,

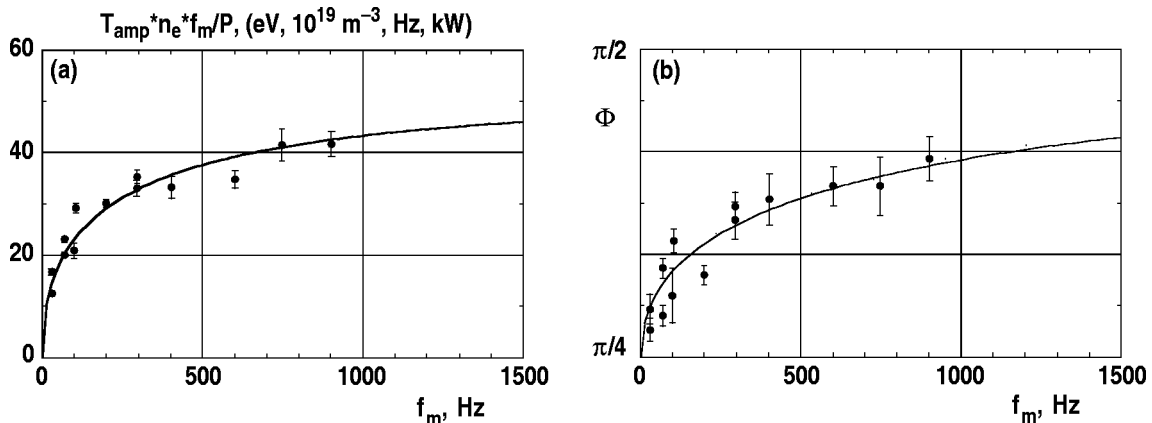


FIG. 7. From ASDEX Upgrade, scan of ECH modulation frequency for a case with narrow deposition profile in a low diffusivity region of the plasma: (a) normalized amplitude $T_{amp} n_e f_m / P$, where T_{amp} is the amplitude of the temperature fluctuation at the modulation frequency f_m , n_e is the density, and P is the ECH power, and (b) phase of the local temperature response. The lines are a best fit to the model from which a deposition width of 2.3 cm was inferred, where TORBEAM predicts 1.0 cm. The inferred diffusivity of $1.18 m^2/s$ is consistent with the diffusivity from power balance. Reprinted from Ref. 68.

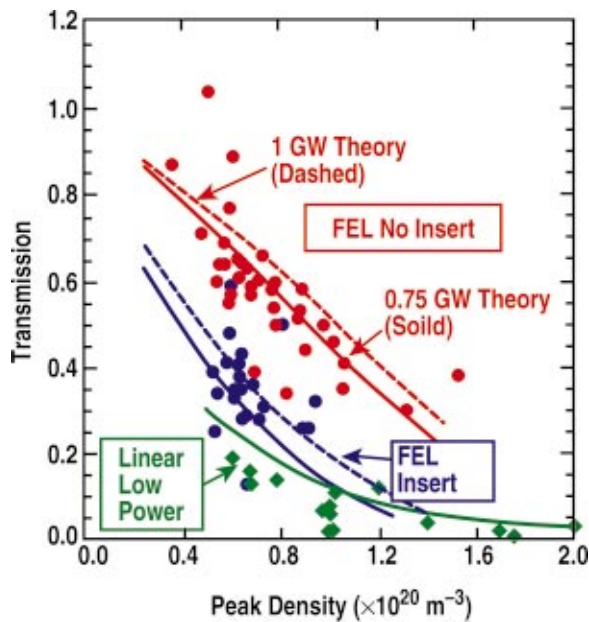


FIG. 8. (Color) Transmission measurements as a function of peak density from MTX, where the free electron laser power source reached 1 GW for pulses of 20 ns duration. The measurements at high power (red circles) show much higher transmission than at low power (green diamonds), indicating nonlinear effects. In the case with the “FEL insert,” the n_{\parallel} spectrum is broadened by means of a narrowed waveguide insert, and agreement with linear theory is recovered even at high FEL power. For the high power cases the theory curves represent calculations using an orbit following code. Reprinted from Ref. 70.

shown in Fig. 8, allowed comparison with nonlinear theory showing that for very high power and narrow spectrum of k_{\parallel} the absorption is decreased compared with linear theory but that the linear absorption can be recovered by reducing the power or broadening the k_{\parallel} spectrum.

All of the Fokker–Planck treatments of the wave/particle interaction in tokamaks assume toroidal symmetry, even for the rf source. In practice, however, the ECH power is concentrated at a small number of spots comprising only a few percent of the flux surface area. In the case of toroidal symmetry the wave fields must be reduced from their level in the beam so that the total power is constant. In order to test the validity of the quasilinear toroidally symmetric approach, a Monte Carlo calculation was performed by Harvey⁷¹ to determine the effective rf diffusion coefficient for comparison with that in the Fokker–Planck codes. This work showed that for the condition used (typical of DIII-D or ASDEX Upgrade) the toroidally symmetric approach was suitable for the power in a single beam up to 2 MW. For larger devices like ITER this condition is more easily met, but for smaller devices this issue remains a question.

Measurements of the behavior of the plasma energy can also provide a measure of the integrated absorption, although information about the location of the interaction is lost. For example, measurements of the single-pass absorption of the X3-mode on TCV were done using the novel technique of modulated ECH with the response measured by the diamagnetic loop,^{35,72} using X2-mode preheating. These measurements, which used the X3-mode launched from the low field side, showed better heating efficiency than expected from the

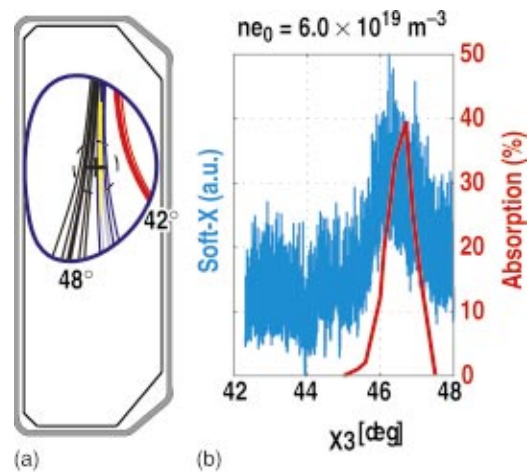


FIG. 9. (Color) (a) Calculated ray trajectories in TCV as a function of mirror steering angle for top launch of the X3-mode. (b) Soft x-ray response from the plasma, indicating the plasma heating and its sensitivity to the launch angle. The red line is the calculated absorption using the TORAY-GA code. The peak density is well above the X2-mode cutoff. Reprinted from Ref. 75.

linear ray tracing calculations. This was attributed to an excess of energetic electrons developed by the X2-mode preheating. In more recent work,⁷³ the absorption of the X3-mode was increased by using a top launch for which the ray trajectories are nearly parallel to the resonance. This approach increases the $B/(dB/ds)$ factor in Eq. (17) as a means of increasing the optical depth, but it has the deficits of weak localization and control of the heating profile since the refraction is sensitive to the launching geometry and the absorption is sensitive to the density and temperature profiles. This sensitivity to launch angle can be seen in Fig. 9,^{74,75} which has motivated the TCV group to develop a real-time feedback control system for the mirror angle in order to maintain optimum coupling. The X3-mode offers the opportunity for broad plasma heating at high density in TCV (Fig. 2). In experiments the measured absorption in high density ($5 \times 10^{19} \text{ m}^{-3}$) ohmic plasmas was 65% to 85%.⁷³ A small nonthermal tail in the electron distribution can improve this to full absorption in many cases in TCV, and in fact the location of the absorption of the X3-mode can be controlled through the placement of the superthermal electrons by X2-mode heating.⁷⁶

Measurements of integrated absorption or of the plasma response can also be used to validate mode purity. Systematic comparisons of O1-mode purity were reported on JT-60U using central response of the electron temperature as a measure,¹⁹ and also on TCV using the diamagnetic loop to measure the plasma response to the X3-mode power using the X2-mode to preheat the plasma.⁷² On the FTU tokamak measurement of the residual power using probes in ports has been used to validate the mode purity.⁷⁷

Measurements with modulated ECH and with transmission measurements have generally shown good agreement with the applicable theory. It turns out, as will be shown in Sec. III E, that the ability of EC waves to drive current is quite sensitive to the magnitude of the absorption coefficient, so comparison of experiment and theory for ECCD is addi-

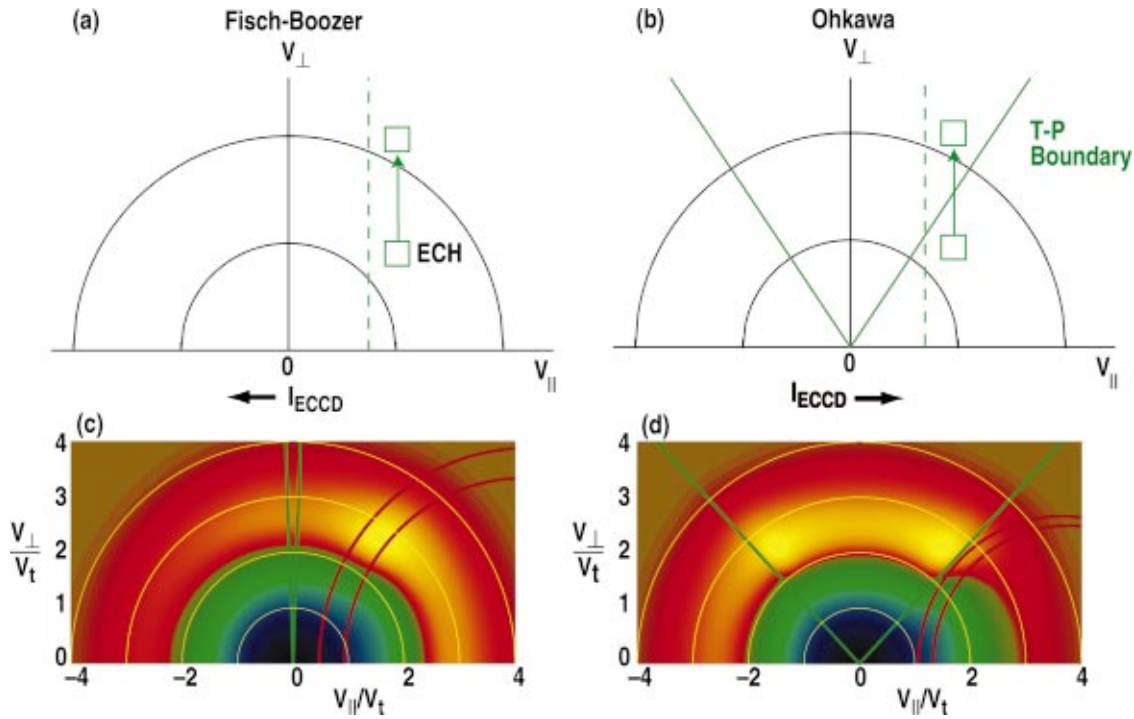


FIG. 10. (Color) (a) Schematic illustration in velocity space of electron cyclotron current drive by the Fisch–Boozer process (Ref. 79) in a linear geometry and (b) by the Ohkawa process (Ref. 78) in a toroidal geometry. Using the CQL3D Fokker–Planck code which will be discussed later, (c) net changes in the electron distribution function for a wave/particle interaction on the high field side of a tokamak where trapping is minimal to illustrate the effects of the Fisch–Boozer process, and (d) same for a wave/particle interaction on the low field side to illustrate the Ohkawa process. The cool colors represent a decrease in the distribution function and the warm colors represent an increase. The normalized minor radius is 0.75, and n_{\parallel} is chosen to maximize the magnitude of driven current in both cases [for (c) $n_{\parallel}=0.28$ and for (d) $n_{\parallel}=0.24$].

tionally a sensitive quantitative test of the absorption physics.

III. ELECTRON CYCLOTRON CURRENT DRIVE (ECCD)

Electron cyclotron waves can drive current in a toroidal plasma, as pointed out by Ohkawa⁷⁸ and by Fisch and Boozer⁷⁹ well in advance of experiments on the topic. As we have seen, the wave absorption may be highly localized in space near the intersection of the wave with the resonance, so that the driven current may also be localized in a robustly controllable manner. This unique localization and controllability offer the opportunity to apply ECCD to tasks such as using the driven current to interact with MHD modes localized near rational surfaces in tokamaks as well as tasks needing less localization like control of the current profile or even sustainment of bulk current in tokamaks or modification of the bootstrap and Pfirsch–Schlüter current profile in stellarators which may be needed to control the radial profile of rotational transform.

In Sec. III A the basic physics behind ECCD is described. In Sec. III B the dimensionless current drive efficiency is defined and the methods used to calculate ECCD are described and applied to two cases, one of weak absorption and one of strong absorption, as a way to illustrate the improvement of ECCD efficiency when the β_e is increased. The detailed interaction of the wave with electrons in velocity space is discussed in Sec. III C, again illustrated by the low and high β_e cases. Techniques for measurement of

ECCD in experiments are presented in Sec. III D and the comparisons between experiment and theory are in Sec. III E.

A. Fisch–Boozer and Ohkawa current drive

Two effects are responsible for the current, and both rely on the absorption of EC waves which have a toroidal propagation component ($n_{\parallel} \neq 0$) and strong damping so that the waves are fully absorbed by electrons with a single sign of v_{\parallel} . One effect, found by Fisch and Boozer,⁷⁹ considers the perpendicular excursion in velocity of a group of electrons with positive v_{\parallel} . These electrons are accelerated to higher energy and hence to a less collisional location in velocity space, since the collision rate declines as v^{-3} . The collisional relaxation process—primarily pitch angle scattering—symmetrizes the high energy electrons more slowly than it fills the lower energy location they came from. In the limit of a steady-state process, this leaves an excess of electrons with positive v_{\parallel} , and hence a current in the negative toroidal direction. This is illustrated in Fig. 10(a). The other effect, found earlier by Ohkawa,⁷⁸ may be important in the case of a toroidal plasma with a trapping region in velocity space generated, for example, by the radial decrease in the toroidal field of a tokamak. If the effect of the EC-induced velocity excursion is to move electrons with positive v_{\parallel} from the passing region to the trapped region as shown schematically in Fig. 10(b), then the v_{\parallel} asymmetry of those electrons is very rapidly lost due to bouncing in the magnetic well. In steady state the electron collisional flux out of the trapped

region balances the EC-driven flux into the trapped region, but the detrapping process is symmetric in v_{\parallel} while the trapping process is asymmetric. This leaves a deficit in velocity space at the original location of the electrons and an excess of electrons with the opposite sign of v_{\parallel} , generating an electrical current in the positive toroidal direction.

For ECCD the Fisch–Boozer and Ohkawa currents are in opposite directions, as shown in Figs. 10(a) and 10(b), so the physics which determines the balance must be carefully considered. The first kinetic calculations that accounted for both effects analytically are described in Refs. 80 and 81. A widely used linear computational model developed by Cohen⁸² is based on a Green's function formulation of current drive with the magnetic field approximated as a square well in order to obtain an analytic solution. The collision operator is valid only in the high velocity limit and does not conserve momentum in electron–electron collisions, which leads to an underestimate of the driven current, and a simplified model of the rf quasilinear diffusion operator in which the wave polarization is assumed to be purely E_{-} is used. The Cohen model is used in the TORAY-GA and TOR-BEAM codes for calculation of the driven current. The TORAY-GA code may also use an alternate version of the Cohen model developed by Lin-Liu *et al.*⁸³ which uses arbitrary magnetic geometry instead of the square well approximation and uses fully relativistic electron dynamics; however, the results of the two models are very similar. As we will see below, many of the physics limitations of the linear models are avoided in Fokker–Planck models. However, the Fokker–Planck calculations are time consuming and impractical for some purposes such as analysis between discharges or surveys to optimize the launching geometry. [Figures 10(c) and 10(d) will be discussed in Sec. III C.]

Current drive by means of toroidally propagating electron cyclotron waves may seem counter-intuitive, since the toroidal momentum introduced by EC waves is negligible due to the high frequency of the waves. In the Fisch–Boozer case the electron current is due to a collisional momentum balance between ions and electrons such that toroidal momentum is conserved, making the current drive a self-consistent steady state process. The Ohkawa current drive is more complicated. When an untrapped electron traveling in the direction which would generate a co-current becomes trapped (and thereby generates a counter-current as discussed above), its guiding center also takes a small radial step inward due to the nature of trapped and untrapped orbits. This particle pinch conserves canonical angular momentum which results in an increase in the vector potential. But a net inward flow of particles cannot be a steady-state process. When the electron eventually moves radially outward as it must for a steady-state density profile, the stored vector potential may be expressed as an enhanced bootstrap current. A fully self-consistent theory of the Ohkawa current including the particle flows and radial electric fields has not been made, although the bootstrap current resulting from measured density profiles is accounted for. The experiments in Sec. III E suggest that in present devices the Ohkawa current is well calculated ignoring the radial electron flows, which are not included in any current drive calculations described in this

paper. Typically the radial step size, the electron poloidal gyroradius, is two or three orders of magnitude smaller than the density scale length, so it is possible that the effect may be lost in the presence of even small deviations from axisymmetry. A comprehensive code which follows an ensemble of electron orbits may be needed to address this issue.

B. Current drive efficiency

The driven current per power for a plasma in a constant magnetic field and with the current drive interaction at a velocity near v_t may be written as^{3,61}

$$\frac{I_{EC}}{P_{EC}} = \frac{\varepsilon_0^2}{e^3} \left(\frac{kT_e}{\ln \Lambda R n_e} \right) \zeta \left(n_{\parallel}, \frac{kT_e}{mc^2}, \frac{\omega_p^2}{\Omega_e^2}, M_B, Z_{eff} \right),$$

where I_{EC} is the driven current, P_{EC} is the absorbed power, ε_0 is the permittivity of free space, $\ln \Lambda(n_e, T_e, Z_{eff})$ is the Coulomb logarithm, and R is the major radius. The dimensionless function ζ includes effects associated with the magnetic mirror ratio M_B , interaction velocities not near v_t , the details of the wave/particle interaction, and the effect of Z_{eff} on collisions. Then, neglecting the weakly varying logarithmic factor, the dimensionless current drive efficiency can be written^{84,85}

$$\zeta = \frac{e^3}{\varepsilon_0^2} \frac{n_e I_{EC} R}{P_{EC} k T_e} \approx 32.7 \frac{n_{20} I_A R_m}{P_W T_{keV}}, \quad (19)$$

where n_{20} is the local density in units of 10^{20} m^{-3} , I_A is the driven current in A, R_m is the major radius in meters, P_W is the power in W, and T_{keV} is the local temperature in keV.

The current drive efficiency described in this truly dimensionless way includes the key dependences on density and temperature. When ECCD is applied at different locations in the plasma, the deviation of ζ from a constant may be attributed to changes in the part of velocity space where the interaction takes place relative to the thermal velocity and the trapping boundary, rather than to the less interesting behavior of I_{EC}/P_{EC} due simply to changes in the collision frequency. This efficiency differs from the conventional current drive figure of merit $\eta = n_e I_{EC} R / P_{EC}$ by being dimensionless and by including the needed dependence on T_e .

In the linear model, the driven current per unit power at each step along the ray is a function of T_e , the parallel index of refraction n_{\parallel} , and the magnetic field geometry. The magnetic fields may be characterized by B_{\max} , B_{loc} , and B_{\min} , where B_{\max} and B_{\min} are the maximum and minimum magnetic field along the flux surface and B_{loc} is the local value. The three parameters expressing the magnetic geometry may be equivalently expressed as the inverse aspect ratio $\varepsilon = (B_{\max} - B_{\min}) / (B_{\max} + B_{\min})$, the quantity $\ell \Omega_e / \omega$ which represents how close the local ray element is to the cold resonance, and the quantity $\theta_{\text{pol}} = \cos^{-1}[(B_{\min} + B_{\max} - 2B_{\min} B_{\max} / B_{\text{loc}}) / (B_{\max} - B_{\min})]$ which represents the “poloidal angle” where the interaction takes place. In the limit of large aspect ratio and circular flux surfaces, θ_{pol} is just the geometric angle between the midplane and a minor radius, with $\theta_{\text{pol}} = 0$ at the outboard midplane. The ratio $B_{\max} / B_{\text{loc}}$ enters the calculation because this quantity determines the

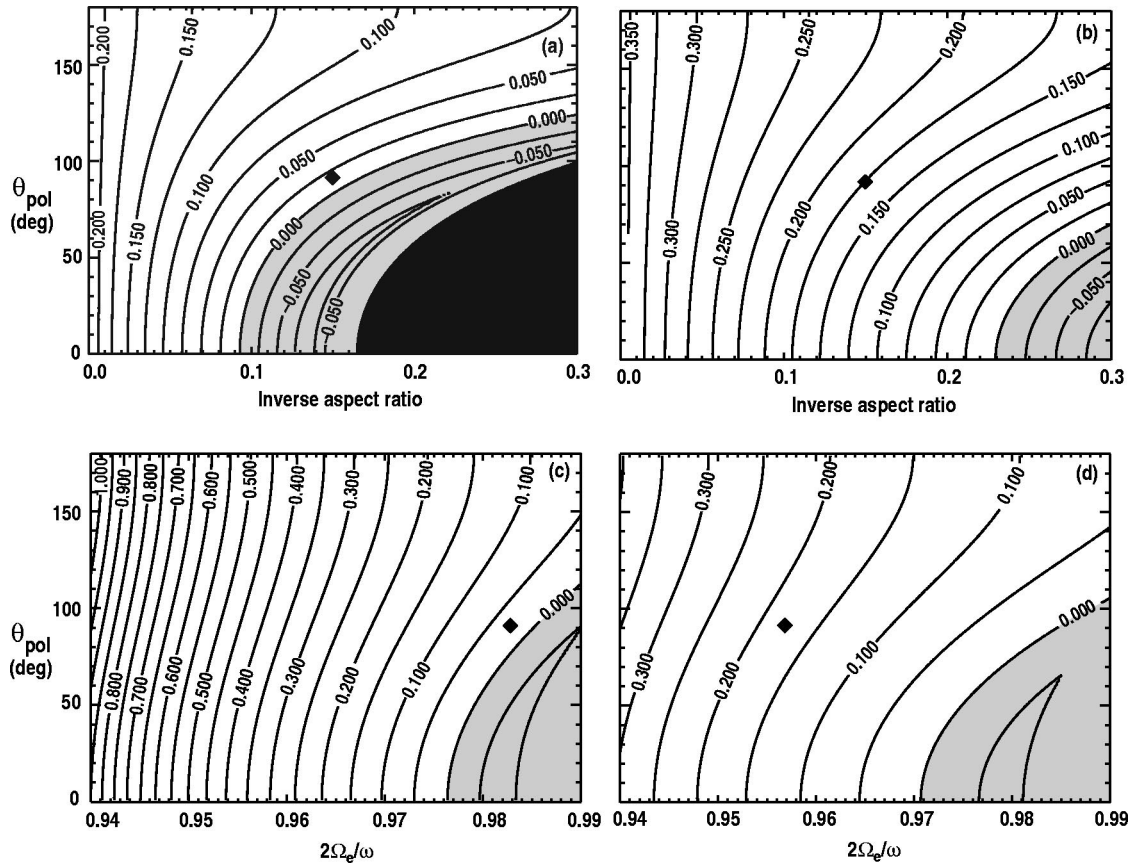


FIG. 11. Contours of dimensionless current drive efficiency, plotted in θ_{pol} and ε space for (a) $\beta_e = 0.19\%$ ($T_e = 1.43$ keV and $n_e = 1.21 \times 10^{19} \text{ m}^{-3}$) and $2\Omega_e/\omega = 0.983$, and (b) $\beta_e = 1.8\%$ ($T_e = 4.3$ keV and $n_e = 3.70 \times 10^{19} \text{ m}^{-3}$) and $2\Omega_e/\omega = 0.957$, and in both cases $n_{\parallel} = 0.38$. Plots (c) and (d) have the current drive efficiency contoured in θ_{pol} and $2\Omega_e/\omega$ space for the corresponding conditions of (a) and (b), with the inverse aspect ratio held fixed at 0.15. The plasma geometry is that shown in Fig. 4.

depth of the magnetic well experienced by electrons at the interaction location, which affects the balance between the Ohkawa and the Fisch–Boozer currents. The ratio $B_{\text{max}}/B_{\text{min}}$ enters because this ratio determines the total trapped particle fraction with which the untrapped electrons experience friction.

The density dependence of the current drive is taken from the normalization described above. But since we are interested in the locations along the ray where the absorption is strong, the density also enters indirectly through the parameter $\ell\Omega_e/\omega$. This parameter is affected by the density and temperature because the wave absorption rate increases with n_e and T_e (for all modes except the X1-mode) as described in Sec. II F. The stronger the absorption rate, the further from unity $\ell\Omega_e/\omega$ will be, so the wave absorption will take place further from the cold resonance. This means that the Doppler shift must be larger, so for the same n_{\parallel} and v_i the v_{\parallel} must be larger for resonant electrons. This implies an increase in ζ (although not necessarily in $I_{\text{EC}}/P_{\text{EC}}$) both because the wave/particle interaction is taking place at larger velocity and because the resonance curve has moved further from the trapping boundary as described in Sec. II G and illustrated in Fig. 5.

The effects of driving current at different locations in physical space—as parametrized by θ_{pol} and ε —can be seen from the Green’s function model.^{82,83} Figure 11 shows con-

tours of current drive efficiency [from Eq. (18)] as a function of these parameters calculated for the X2-mode in the DIII-D geometry shown in Fig. 4, assuming constant values of n_{\parallel} , T_e , n_e , and $2\Omega_e/\omega$. In practice these quantities will vary, but the figures illustrate the expected general dependences. Figure 11(a) is for plasma conditions of low β_e corresponding to the “1n1T” resonance curve of Fig. 5, and Fig. 11(b) corresponds to the “3n3T” curve. From the actual ray tracing calculations the location of peak absorption can be determined, and the values at this location are shown in Fig. 11 as the data point, and the contours are calculated using the value of $2\Omega_e/\omega$ determined at that location. The region of this parameter space in which the Ohkawa current dominates is shown as the shaded region. This region shrinks at larger β_e , which can be seen by comparing Figs. 11(a) and 11(b), and this is attributable to the movement of the resonance away from the trapping boundary as shown in Fig. 5. In the regions shaded black there is essentially no current drive as the wave/particle interaction is nearly exclusively with trapped electrons.

The importance of the value of $2\Omega_e/\omega$ in the dimensionless current drive efficiency may be seen in Figs. 11(c) and 11(d). For these contours of current drive efficiency the inverse aspect ratio ε is held fixed at 0.15, corresponding to a normalized minor radius of 0.375, and again n_{\parallel} , T_e , and n_e are held fixed. As in Figs. 11(a) and 11(b), the ray tracing

values are shown as the data points and the curves are calculated using values corresponding to those from the ray tracing. For the low β_e case varying θ_{pol} from 0 to 180° creates a huge difference in the current drive efficiency ζ , which goes from -0.07 at $\theta_{\text{pol}}=0$ to zero at $\theta_{\text{pol}}=80^\circ$ and to 0.12 at $\theta_{\text{pol}}=180^\circ$. On the other hand, for the higher β_e case, ζ is a much weaker function of θ_{pol} , going from 0.13 at 0° to 0.23 at 180° . Larger optical depth helps to tilt the balance between the Ohkawa current and the Fisch–Boozer current toward the latter.

In existing tokamaks it may be advantageous for ECCD at very large values of normalized minor radius to emphasize the Ohkawa current instead of the Fisch–Boozer current by placing the interaction on the low field side rather than the high field side where trapping is minimized.⁸⁶ Calculations show that this approach is suitable for present day devices, but it seems unworkable in devices with very large optical depth (high density, temperature, or physical size) except possibly very near the plasma edge.

C. Interaction in velocity space

For the understanding of the balance between the Fisch–Boozer current and the Ohkawa current it is essential to understand the effect of the EC wave on electrons. All electrons with velocity on the resonance curve satisfy the resonance condition, but the power of the wave is not distributed equally among them. It has been shown above that for all modes except the X1 at low density, the power absorption is a finite Larmor radius effect. For that reason, electrons lying near the $v_\perp=0$ axis are not effectively heated, even though the highest density of electrons along the resonance in velocity space lies at the minimum of v_\parallel where $v_\perp=0$.

From the description above it is clear that the direction of the quasilinear diffusion in velocity space is important in evaluating the current drive process. For the O1-mode, for example, we have seen that the dominant wave/particle interaction is with the parallel component of the wave electric field, which might be expected to lead to a parallel diffusion. However, it can be seen from the principles of conservation of energy and momentum that the diffusion is always in the nearly perpendicular direction. Following Kennel and Englemann,⁸⁷ we use the relativistic expression for the energy, $W^2 = m^2 c^4 = p^2 c^2 + m_0^2 c^4$, to note that

$$\delta W = \vec{v} \cdot \delta \vec{p} = v_\perp \delta p_\perp + v_\parallel \delta p_\parallel, \quad (19)$$

where p_\parallel and p_\perp are the parallel and perpendicular electron momenta. Applying the quantum mechanical concepts that for a quantum interaction between the wave and the particle, the energy transfer is given by $\delta W = \hbar \omega$ and the parallel momentum transfer is $\delta p_\parallel = \hbar k_\parallel$, the energy change can be written

$$\delta W = (\delta W / \delta W_\parallel) \delta W_\parallel = (\hbar \omega / v_\parallel \hbar k_\parallel) v_\parallel \delta p_\parallel. \quad (20)$$

Combining Eqs. (19) and (20) gives

$$\frac{\delta p_\perp}{\delta p_\parallel} = \left(\frac{\omega}{k_\parallel v_\parallel} - 1 \right) \frac{v_\parallel}{v_\perp}. \quad (21)$$

Typically the parallel phase velocity ω/k_\parallel is much larger than the speed of light for EC waves, so $\omega/k_\parallel v_\parallel$ is a large number. Then except very near the $v_\parallel=0$ axis we have $\delta p_\perp \gg \delta p_\parallel$, so for both X- and O-modes the diffusion is primarily in the perpendicular direction. This is a seemingly paradoxical result for the O-mode since it was shown above that for this mode the parallel component of the wave electric field changes the electron parallel energy. However, the interaction of the electron with the wave magnetic field—which does not affect the electron total energy—is responsible for converting between parallel energy and perpendicular energy in order to satisfy the conservation of energy and momentum.⁵⁶

A Fokker–Planck computer code may be used to determine the details of the wave/particle interaction in velocity space. For an extensive discussion of relevant Fokker–Planck physics and codes see the comprehensive reviews by Karney⁸⁸ and by Westerhof⁸⁹ and the references therein. Commonly used Fokker–Planck codes include CQL3D,⁹⁰ BANDIT-3D,⁵¹ and the code by Giruzzi.⁹¹ The regime of interest has the periodic gyro and bounce motion of the electrons much faster than the collision time, so $\Omega_e \gg \nu_b \gg \nu_{\text{coll}}$, where ν_b is the bounce time and ν_{coll} is the collision frequency, and the time scale of interest is much longer than ν_{coll}^{-1} . In steady-state the diffusion in velocity space due to collisional relaxation balances the source terms of the bounce-averaged Fokker–Planck equation,

$$C(f_0) = D_v(f_0) + E_{dc}(f_0). \quad (22)$$

Here $C(f_0)$ is the collision operator acting on the electron distribution function f_0 which is evaluated at the minimum of the magnetic well where the magnetic field is B_0 , and $E_{dc}(f_0)$ is a source of diffusion due to a parallel steady-state electric field. The quasilinear diffusion tensor due to the EC wave is the relativistic generalization⁸⁹ of that derived by Kennel and Englemann.⁸⁷ The component giving radial diffusion in velocity space—heating, that is—is given by^{89,90}

$$D_{vv} = \frac{\pi e^2 \sin^2(v_\parallel / v_\perp)}{p_\perp^2 |v_\parallel|} \sum_j G_j \Delta(k_\parallel - k_j). \quad (23)$$

Here,

$$\Delta(k_\parallel - k_j) = \begin{cases} 1/\Delta k_\parallel & \text{for } |k_\parallel - k_j| < \Delta k_\parallel / 2, \\ 0 & \text{for } |k_\parallel - k_j| \geq \Delta k_\parallel / 2, \end{cases} \quad (24)$$

$k_j = (\omega - j\Omega_e / \gamma) / v_\parallel$ is the resonance condition for the j 'th harmonic, Δk_\parallel is the spread of k_\parallel for the ray element, and the relativistic analog of Eq. (16) is

$$G_j = \left| \frac{1}{2} p_\perp E_+ J_{j+1} + \frac{1}{2} p_\perp E_- J_{j-1} + p_\parallel E_\parallel J_j \right|^2. \quad (25)$$

Note that diffusion due to the E_+ component of the electric field is not zero but two orders higher in the Bessel function than for the E_- component.

An output of the bounce-averaged Fokker–Planck code is the steady-state quasilinear distribution function which results from the balance between the EC and electric field effects and collisional relaxation. The ECCD is calculated from the first moment of the distribution function. The CQL3D Fokker–Planck code uses a “mildly relativistic” model for

Coulomb collisions⁹⁰ accurate when the thermal velocity is nonrelativistic, $v_t \ll c$, which is the case in the work presented here. The code calculates the distribution function at the magnetic field minimum, but the distribution function may be evaluated at the spatial location of the wave-particle interaction by scaling to the magnetic field B_{loc} at that location preserving energy and magnetic moment for each element of phase space. This procedure eliminates from the resultant distribution function those electrons which do not reach that magnetic field because they are reflected at lower field and therefore do not participate directly in the interaction, but it provides a self-consistent picture of the resonance, the local trapped particle boundary, and the effects on the distribution function at the spatial location where the interaction takes place.

The changes in the distribution function provide insight into the current drive process. For example, the changes in the distribution function from a Maxwellian at fixed electron temperature due to the wave/particle interaction are illustrated in Figs. 10(c) and 10(d). Figure 10(c) is the change in the distribution function δf due to a wave intersecting the resonance in a DIII-D-like plasma on the high field side at large normalized minor radius of 0.75. In this case the magnetic well depth is minimal, so the Ohkawa effect is virtually absent. The figure shows an enhancement of the distribution function for v_{\parallel}/v_t in the range 1 to 2 and $v_{\perp}/v_t \approx 2$, with a deficit in the same region of v_{\parallel} but small v_{\perp} . Recalling that the phase space plot is a two dimensional slice through a three dimensional distribution with symmetry about the $v_{\parallel} = 0$ axis so that the volume elements increase with v_{\perp} , the net effect is an excess of electrons with positive v_{\parallel} and hence a current in the negative parallel direction. In the case with dominantly Ohkawa current as illustrated in Figs. 10(b) and 10(d), there is an increase in the distribution function near the same v_{\perp}, v_{\parallel} coordinates, but in this case the increase lies inside the trapped region where the bounce process forces exact symmetry in v_{\parallel} and hence these electrons produce no parallel current. Instead, the reduction in density in the positive v_{\parallel} direction and the enhancement in the negative v_{\parallel} direction in the region of 2 to 3 v_t generates an electrical current in the positive parallel direction.

The fluxes in velocity space responsible for the net modification of the distribution function are calculated by CQL3D and can provide insight into the physics of ECCD. The flux is defined as $\vec{\Gamma} = \vec{D} \cdot (\partial f / \partial \vec{v})$, where f is the distribution function and \vec{D} is the quasilinear diffusion tensor, a component of which is given in Eq. (23). Figure 12 shows the fluxes calculated for two cases, with low and high β_e (again corresponding to the extreme cases shown in Fig. 5). In the low β_e case the peak interaction takes place near the trapping boundary, as shown in Fig. 12(a). The flux due to the EC wave is mostly in the v_{\perp} direction, as expected from Eq. (21), and takes place only for a single sign of v_{\parallel} , as needed for current drive. The total flux shown in Fig. 12(b) shows that the interaction with the trapped particle region is strong. On the other hand, for higher β_e the rf flux takes place far from the trapping boundary, as shown in Fig. 12(c) and as expected from the discussion of Fig. 5 above. But the

continuity equation in velocity space requires that the divergence of the flux be everywhere zero for steady state. In the Fokker–Planck equation the flux is made divergence-free by the collisional relaxation, resulting in vortices in velocity space. These can be seen in the flux plot of Fig. 12(d), or more clearly in Fig. 12(e), which is the same data as in Fig. 12(d) except the length of the arrows is proportional to the logarithm of the flux rather than the magnitude of the flux. The vortices are global in scale and link the resonant flux to the trapped particle region. This shows that even though the EC interaction may be made far from the trapping region, the interaction with the trapped particles may still be important.

It may be noted from Fig. 12(d) that the EC interaction creates a total flux which is well suited to generating ECCD. The total flux is nearly in the radial direction in velocity space, which is needed because the Fisch–Boozer effect depends on changes in the collisionality brought on by the acceleration of a group of electrons with a single sign of v_{\parallel} to higher energy and therefore to lower collisionality. If the absorption were not a finite Larmor radius effect as it is for the O1- and X2-modes, the flux would be nearly vertical but peaked near $v_{\perp} = 0$ where the distribution function along the resonance is largest, so the diffusion in velocity space would be parallel to the contours of constant energy rather than across them. Additionally, the total flux has a significant component toward higher v_{\parallel} which aids in generating current, and the total flux is mostly parallel to the trapping boundary rather than across it. A combination of the finite Larmor radius effect and suitable choice of n_{\parallel} can be used to deliberately maximize the flux across the trapping boundary and optimize the Ohkawa component in some cases,⁸⁶ with the beneficial effects of increased current density and reduced requirements on the frequency of the EC power.

The curve representing the driven current per unit ray length, dI/ds , in Fig. 4(c) may now be clearly understood.⁹² When the power is absorbed far from the trapping boundary, the Fisch–Boozer current is dominant and dI/ds is positive. As the ray propagates closer to the cold resonance, the resonance curve moves closer to the trapping boundary and the Ohkawa current starts to compete, eventually dominating where dI/ds is negative. When the resonance has moved so far that the interaction takes place primarily with electrons that are already trapped, no current is generated and dI/ds drops rapidly to zero.

Much greater net current can be obtained with plasma parameters giving greater optical depth, since the wave power may be depleted before the competition becomes severe. This can be seen in Fig. 13, which shows the same information as Fig. 4(c) but for the case with three times higher temperature and density. In this case the wave is fully absorbed well before the resonance is reached (i.e., $2\Omega_e/\omega > 1$) since the wave absorption is so much stronger under these conditions. This larger Doppler shift moves the interaction in velocity space far from the trapping boundary, making dI/ds positive everywhere by reducing the competition from the Ohkawa current.

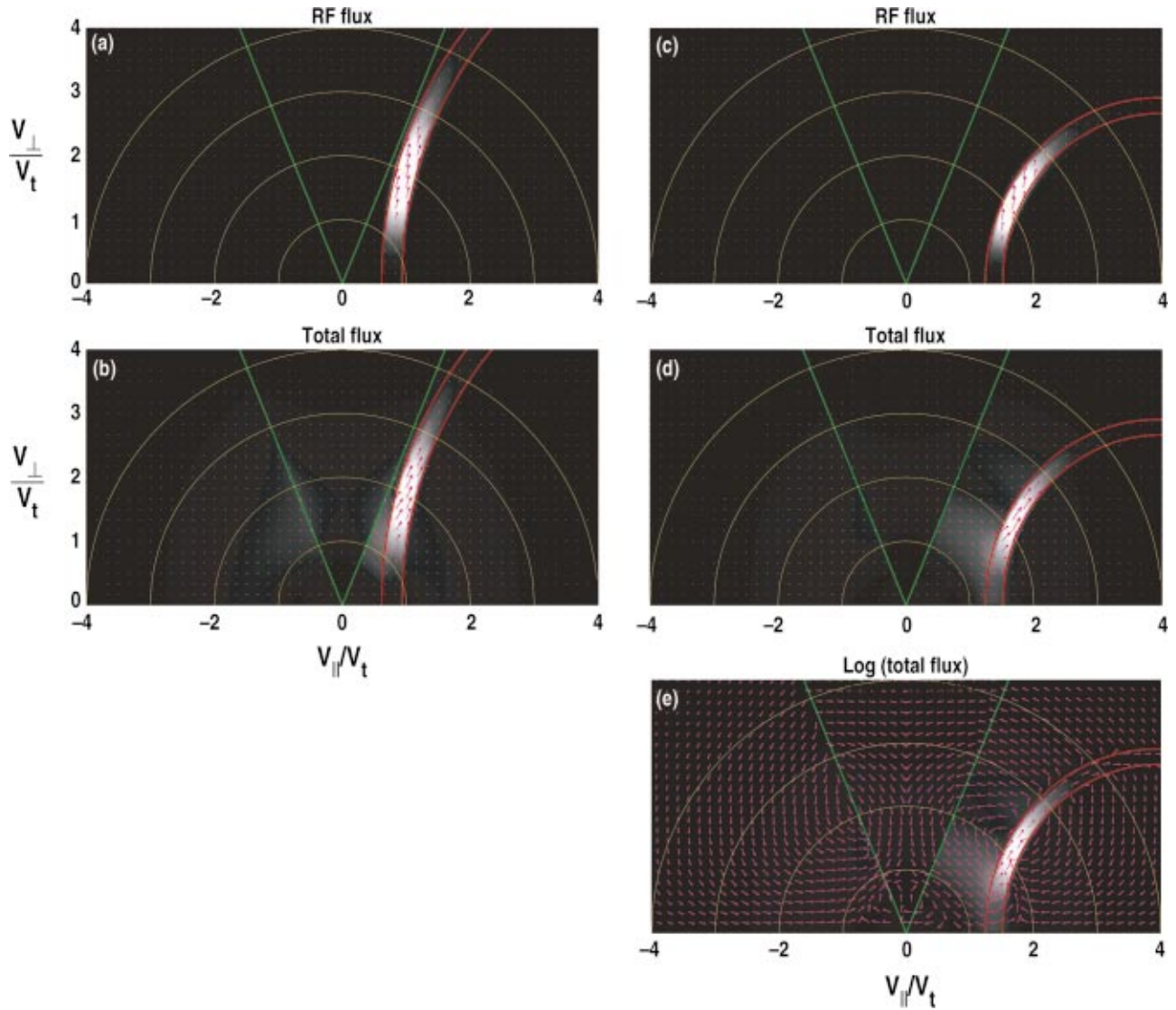


FIG. 12. (Color) Flux in velocity space calculated by the CQL3D code, (a) and (b) for the plasma and conditions shown in Fig. 4, and (c)–(e) for a plasma with three times higher temperature and density. (a) Flux due to the EC wave near the surface of maximum interaction strength, and (b) the total flux when both the EC wave and collisions are included. The arrows indicate the magnitude and direction of the flux, and the brighter white shading indicates larger magnitude. (c) and (d) are the same as (a) and (b) except calculated for a higher density and temperature case corresponding to the “3n3T” curve in Fig. 5. (e) is the same as (d) except the arrow lengths represent the log of the magnitude of the flux. The green lines are the local trapping boundary and the red lines are the resonance at each side of the radial zone used in the calculation. The yellow circles are contours of constant energy. The dc electric field is zero in these calculations and the EC wave is in the X2-mode.

D. Techniques for measurement of ECCD

ECCD in a tokamak can be estimated by comparing the loop voltage necessary to sustain the toroidal current with and without the applied EC power. This approach requires that the increase in conductivity due to the increase in T_e when the EC power is applied be compensated in the model. Better results are obtained by comparing discharges with co-ECCD and counter-ECCD to remove most of the difference in temperature. This determination of the driven current is subject to a rather high degree of uncertainty, particularly if MHD activity is present, but it has been used in many experiments.^{5–8} In recent experiments in the TCV tokamak the uncertainty was eliminated by driving a current larger than the total tokamak current for a time long compared to the time for radial relaxation of the toroidal electric field.^{93,94}

This reduces the loop voltage to a negative value, recharging the Ohmic heating transformer. When the fully relaxed loop voltage is zero then all of the current is supported by the combination of ECCD and bootstrap current. To the extent that the calculated bootstrap fraction is known or not large the ECCD can be unambiguously determined. Data from an example discharge with ECCD overdrive are shown in Fig. 14. Likewise, in stellarators the loop voltage measurement can accurately determine the total ECCD because the competing equilibrium toroidal currents are absent and sensitive experiments of this type have been reported on the Wendelstein 7AS stellarator.²⁷

The loop voltage method can determine the driven current accurately in some cases, but it cannot determine the profile of the driven current. The ability to measure the cur-

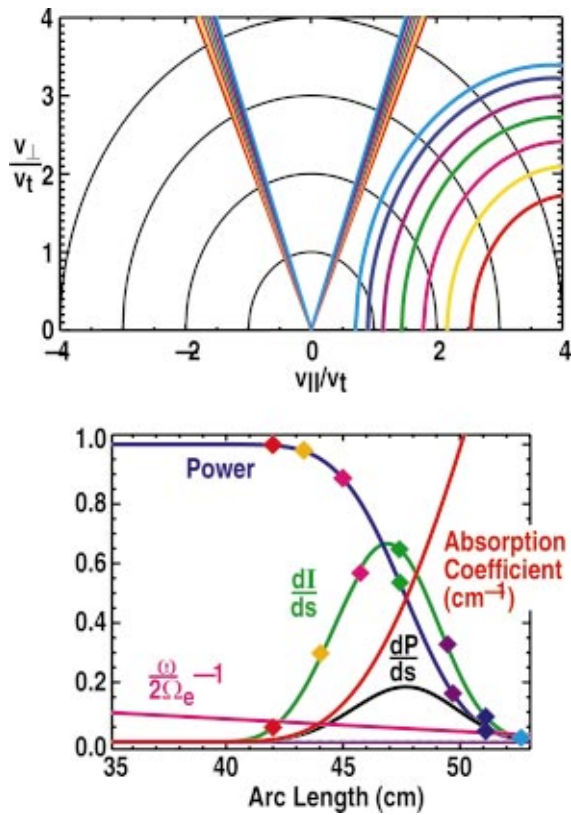


FIG. 13. (Color) Same data as in Fig. 4, except that β_e is nine times higher. (a) Resonance curves (colored curved lines) in velocity space, trapped particle boundary (colored straight lines), and contours of constant velocity (black curves). (b) Power in the ray normalized to the incident power, the power deposition rate $(1/P)(dP/ds)$ (cm^{-1}), absorption coefficient (cm^{-1}), the quantity $\omega/2\Omega_e - 1$, and the deposition rate for electron cyclotron driven current dI/ds (200 A/cm/MW), as functions of length along the ray. The local electron temperature is 4.3 keV and the density is $3.69 \times 10^{19} \text{ m}^{-3}$ at the location of the peak rate of absorption of the ray. These conditions correspond to those of Figs. 12(c)–12(e). The symbols in (b) and the curves in (a) have corresponding colors and are placed at absorbed powers of 1%, 5%, 20%, 50%, 80%, 95%, and 99% of the incident power.

rent locally came with the advent of diagnostics which measure the local magnetic field, such as the motional Stark effect (MSE) diagnostic (for example, Ref. 95). This diagnostic measures the local pitch angle of the magnetic field at a radial array of locations in the plasma. The information from these measurements can be used to constrain the reconstruction of the equilibrium to obtain an accurate map of flux surface contours in the plasma and the radial profile of total current density. Since the local toroidal electric field can be found from the time derivative of the flux, the ohmic current density can again be subtracted from the total current density to obtain the sum of the noninductive currents (i.e., bootstrap current, ECCD, and possibly neutral beam driven currents).⁹⁶

This method is challenging to employ because the width of the radial profile of current density in the ECCD case may be very narrow, a few cm or less, and it is difficult to reconstruct equilibria with this resolution.⁹⁷ This is an even greater problem for diagnostic methods like Faraday rotation which produce only line-integrated measurements of magnetic field. An alternate approach is to compare the measured MSE sig-

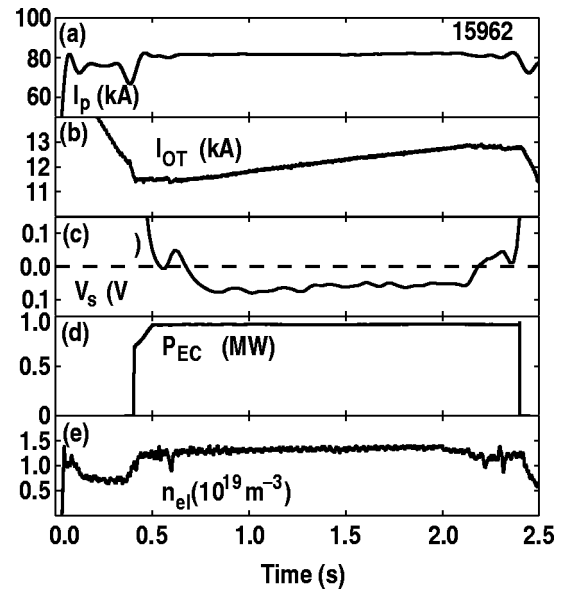


FIG. 14. Recharging of the Ohmic transformer on the TCV tokamak, using 1 MW of incident power with the driven current near the plasma center. The plasma current, the current in the Ohmic transformer, the surface loop voltage, the EC power, and the line averaged plasma density are shown. (Reprinted from Ref. 93.)

nals with simulations of the MSE evolution using a model for the width, magnitude, and location of the ECCD.⁹⁸ The parameters of the model are varied systematically until a minimum in the errors between the fit of the measured MSE signals and the simulated signals is obtained. This process provides determination of the localized features of the current profile up to the resolution of the MSE system. An example of this method of determining the ECCD is shown in Fig. 15. In this discharge from DIII-D, the ECCD is localized between two adjacent channels of the MSE system, or about 5 cm. This clearly illustrates the degree to which ECCD can be localized in actual practice.

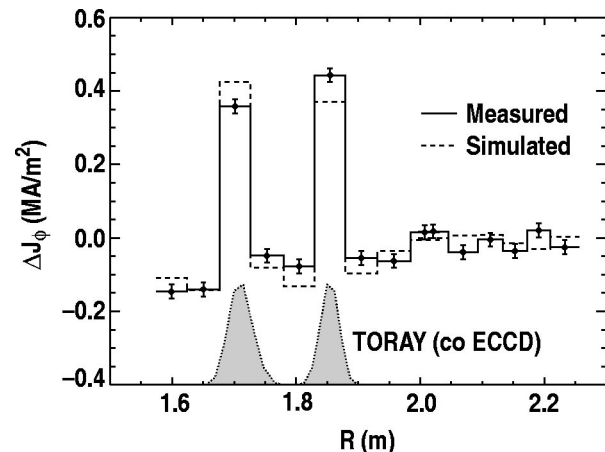


FIG. 15. Change in the measured (solid line) and simulated (dashed line) toroidal current density as a function of major radius between a discharge with co-ECCD and one without EC power, taken from the DIII-D tokamak. (Reprinted from Ref. 85.)

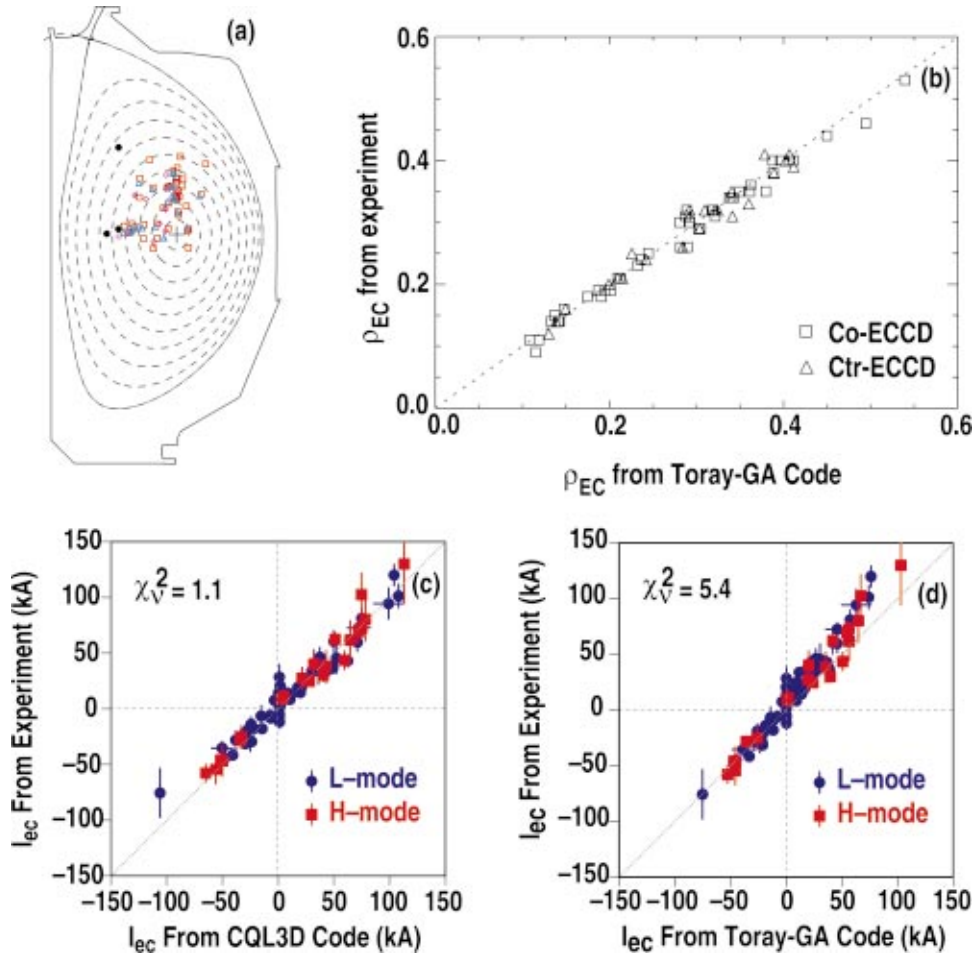


FIG. 16. (Color) ECCD measurements taken from the DIII-D tokamak. (a) Locations of the application of EC power on a plasma cross section. The square points are for co-ECCD, the triangles are for counter-ECCD, and the diamond points are for radial ECH (no current drive). The circle points are the locations of ECCD used in tests of stabilization of MHD activity where unambiguous results of current drive were found but no direct measurement of the driven current was made. (b) The normalized minor radius of the peak of the measured ECCD vs that calculated by TORAY-GA, for all the points of (a) except those with radial ECH. (c) Comparison of measured ECCD vs that calculated by a quasilinear Fokker-Planck code including the effects of $E_{||}$. (d) Comparison of measured ECCD vs that calculated by a linear ray tracing code. [Parts (c) and (d) are reprinted from Ref. 85.]

E. Comparison of ECCD with theory

Detailed measurements of ECCD show excellent agreement with theory,⁸⁵ except in cases where extremely high power density may exhibit nonlinear effects as in Wendelstein 7-AS⁹⁹ and TCv.^{75,100} Figure 16 shows the results of a systematic set of measurements made on the DIII-D tokamak.⁸⁵ The locations of the measurements on the cross section of a typical equilibrium are shown in Fig. 16(a). These measurements include a range in n_e of $1.5\text{--}4.8 \times 10^{19} \text{ m}^{-3}$, in T_e of $1.2\text{--}5 \text{ keV}$, and in $n_{||}$ of -0.46 to 0.55 , with ρ and θ_{pol} as shown in the figure. Figure 16(b) shows that the measured minor radius of the peak in the driven current profile is in excellent agreement with that calculated by the TORAY-GA ray tracing code over the entire range of conditions. In addition to the location, the magnitude of the ECCD is also in excellent agreement with the calculations using the CQL3D Fokker-Planck code, as shown in Fig. 16(c).⁸⁵ In this comparison, the quasilinear effect of the EC power on the plasma conductivity is included. The $E_{||}$ effect is measurable in these discharges, allowing a decrease in the goodness of fit parameter χ^2 from 3.0 to 1.1 over the entire data set. The fit of the DIII-D measurements of the magnitude of driven current to the calculations of the linear ray tracing code TORAY-GA is not as good as the fit as that for CQL3D, yet adequate for many purposes, as shown in Fig. 16(d). In this case the χ^2 is increased to 5.4. The quasilinear model differs from the linear model in that quasilinear effects

on the electron distribution are included in calculating the ECCD, the collision operator conserves momentum in electron-electron collisions, and the effects of $E_{||}$ are included. In a reactor-like plasma, only the momentum conservation effect is likely to be significantly different. Similar tests of ECCD using the loop voltage technique for measurement have been obtained from the T-10 tokamak,⁷ showing good agreement for the X2- and O1-modes. Experiments with co-ECCD on ASDEX Upgrade using the X2-mode have 82% of the total plasma current supported by ECCD,¹⁰¹ verified through comparisons with the ASTRA transport code.

The beneficial effect on the ECCD of increasing β_e can be seen by replotting a selected subset of the data shown in Fig. 16. Figure 17 shows the measured dependence of the dimensionless efficiency on the local value of β_e for a set of discharges with fixed current drive location above the plasma center and $n_{||}$ fixed for co-ECCD. As expected from the discussion in Sec. III B the dimensionless efficiency (which has the expected dependence on n_e and T_e normalized out) increases due to the reduction in the Ohkawa current as the resonance is shifted further in velocity space from the trapping boundary. This effect is stronger when the magnetic well is deeper at larger ρ , as the figure shows. In fact, at the highest β_e used, the current drive efficiency at $\rho=0.4$ approaches that at $\rho=0.3$ as the trapping effects diminish. This is favorable for effective ECCD under reactor-like conditions.

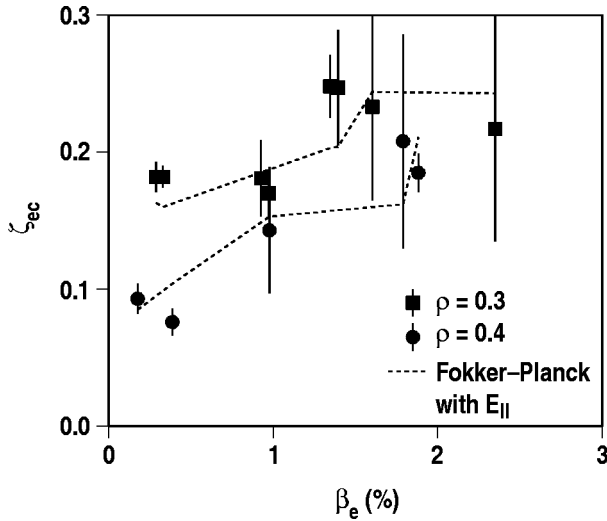


FIG. 17. Measured dependence of the dimensionless ECCD efficiency on the local electron β_e for deposition locations of $\rho=0.3$ and 0.4 , with $\theta_{pol}=85^\circ$ and $n_{||}=0.3$. The results of calculations with the CQL3D code are shown as the dotted lines. (Reprinted from Ref. 85.)

For current drive in ITER the O1-mode is used with electron temperature in the range 10 to 25 keV. Measurements of ECCD with this mode in this temperature range have been made on the JT-60U tokamak,^{102,103} resulting in a record ECCD current of 0.74 MA and validating the physics model under parameters similar to those of a burning plasma. Data from such an experiment are shown in Fig. 18. The total current in this discharge is 0.6 MA, and the neutral beam heating uses balanced beams to minimize the current driven. The central temperature reaches 23 keV when 2.3 MW of co-ECCD and 0.6 MW of ECH are added at a ρ of 0.17. The measured profile of ECCD is in moderate agree-

ment with that from a calculation using a linearized Fokker-Planck code which found an integrated ECCD of 1.1 MA. The resistive diffusion time at these high temperatures greatly exceeds the duration of the experiment, so some of the driven current may be cancelled by the induced back-emf. As the profile of the electric field relaxes the minimum in the safety factor drops and instabilities occur, resulting in the sudden drop in T_e at 5.96 s. The dimensionless current drive efficiency at $\rho=0.35$ with $\theta_{pol}\approx 90^\circ$ was found to be half of that at the high field side midplane, in agreement with the calculations. The normalized current drive efficiency was also found to increase with plasma density, which may be another manifestation of the effects of trapped particles described above.

Measurement of the driven current in the TCV tokamak,^{75,93,94} under the condition common in TCV that the high ECH power density generates a strongly non-Maxwellian electron distribution, is 3 to 10 times smaller than would be expected from calculations using the CQL3D code in the way it was applied in the DIII-D experiments.^{75,100} This discrepancy in the TCV case can be understood by considering radial transport of the energetic electrons which act to drive the current.^{100,104} The discussion of the Fisch-Boozer current given above implies that the current is developed on the time scale of pitch-angle scattering, while electrons are transported radially on the time scale of the particle confinement time. If the ratio of the transport time to the pitch angle scattering time is not large, the driven current will be broadened and possibly reduced. The CQL3D code may be used in a mode which includes radial transport to simulate this effect, using a particle diffusion operator with a velocity dependence which models either electrostatic or magnetic turbulence. For the electrostatic model the cal-

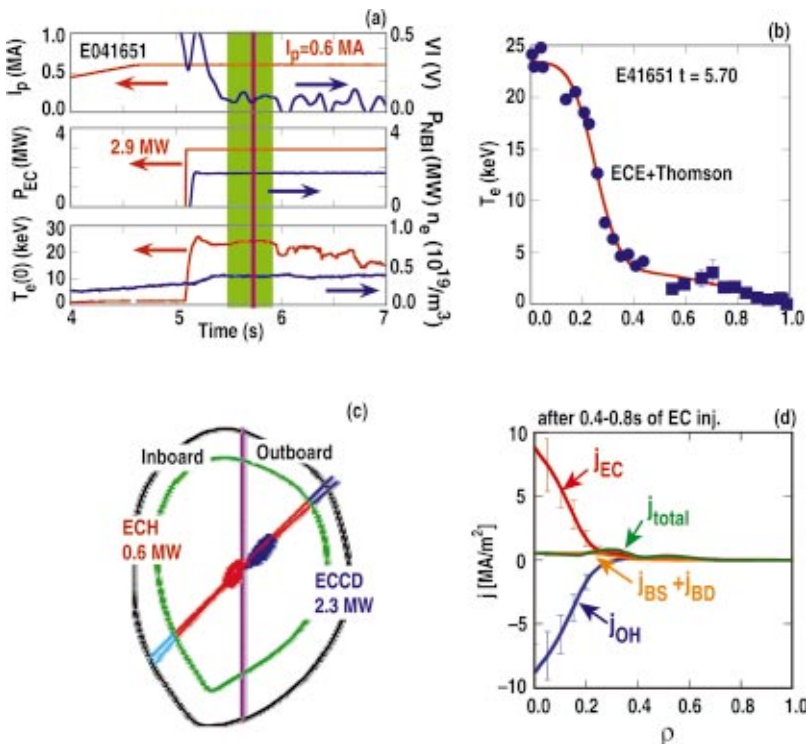


FIG. 18. (Color) Discharge with 0.74 MA ECCD in JT-60U, (a) plasma current and edge loop voltage, ECH and neutral beam power, and central electron temperature and line averaged electron density. The current drive is analyzed during the time marked by the green shading where electron temperature is nearly constant. (b) Electron temperature profile during the ECCD measured by ECE (circles) and Thomson scattering (squares), as a function of normalized minor radius. While ECE is susceptible to recording radiation temperatures that exceed the electron temperature due to a nonthermal component, the temperature is confirmed to exceed 20 keV by Thomson scattering. (c) Deposition location for ECH (red) launched with no toroidal component and for co-ECCD (blue). The vertical line is the cold resonance. The ECH is damped on the high field side because the only resonance broadening mechanism is the relativistic downshift in frequency, while the ECCD is deposited on the low field side because of the Doppler upshift in frequency. (d) Profiles of the components of the current density. (Reprinted from Ref. 103.)

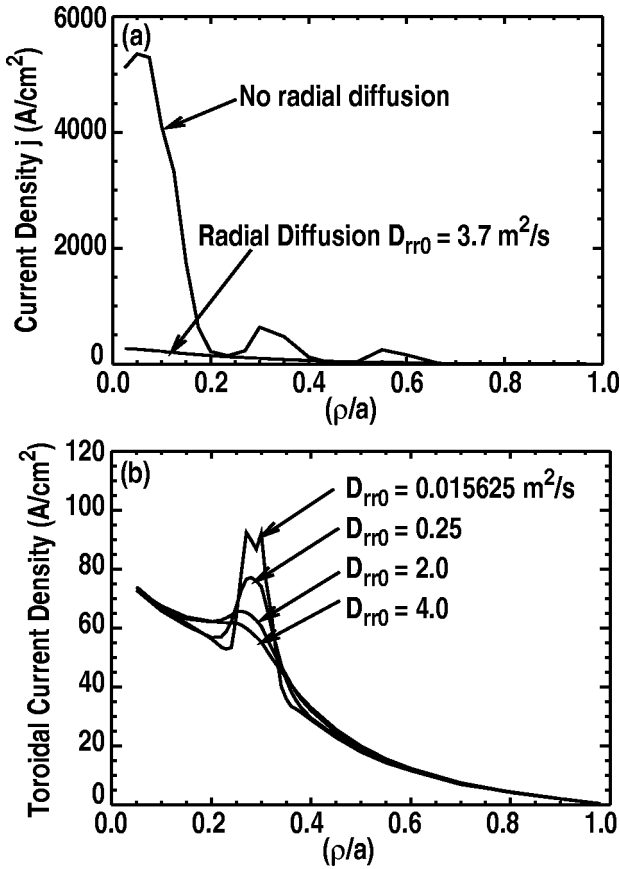


FIG. 19. (a) Calculated radial profile of total current density in TCV, with and without radial diffusion. (b) Same, for DIII-D discharge, for various levels of radial diffusion. The case of $2.0 \text{ m}^2/\text{s}$ matches the ITER L-mode energy scaling. (Reprinted from Ref. 100.)

culated current is reduced from 550 kA to 100 kA, which is close to the measured current, by using a diffusion coefficient of $3.7 \text{ m}^2/\text{s}$. This diffusion coefficient is in reasonable agreement with the energy confinement time in TCV. These results are shown in Fig. 19(a). Applying the same model to a DIII-D discharge using a particle diffusion coefficient consistent with the energy confinement time in that device (roughly $2 \text{ m}^2/\text{s}$) produces a slight broadening of the driven current profile but little net loss of current,¹⁰⁰ as shown in Fig. 19(b). However, this broadening is not observed in the MSE measurements on DIII-D, suggesting that the particle diffusion coefficient including the effects of an inward pinch is an order of magnitude smaller than the energy diffusion coefficient.¹⁰⁵ The magnitude of the reduction of ECCD in TCV, DIII-D, and some other tokamaks was fit to a simple scaling by Luce.⁸

A key difference between the TCV and DIII-D experiments is the power density. The power in the two tokamaks is similar, but the plasma in DIII-D is 15 times larger in volume than that in TCV. The power density in these discharges can be compared with the criterion developed by Harvey *et al.*⁵⁵ for the expected appearance of significant quasilinear effects; that is, where the linear calculations may start to become unreliable and Fokker-Planck calculations are needed. This criterion is $2Q_e/n_{19}^2 > 1$, where Q_e is the heating power per unit volume in units of MW/m^3 averaged

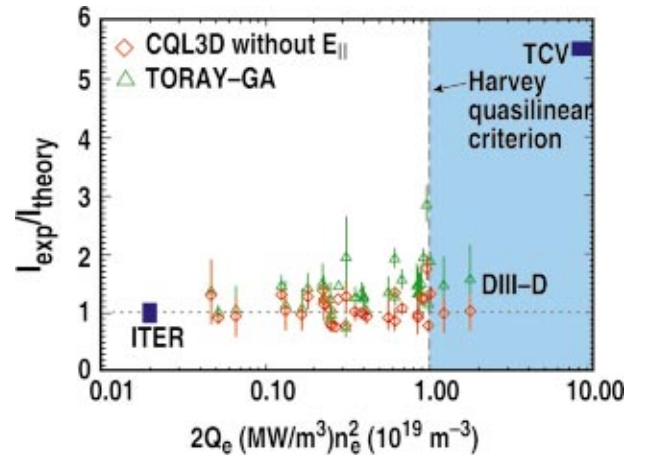


FIG. 20. (Color) Ratio of measured ECCD to the ECCD expected from theory vs the Harvey criterion (Ref. 55) for the onset of quasilinear effects, on a log scale. The full set of DIII-D cases with ECCD greater than 10 kA from Fig. 16 are shown, using the quasilinear code CQL3D (diamonds) and the TORAY-GA code (triangles) as the theory. For the TCV point the ratio of the current calculated by CQL3D to that by TORAY-GA is used, using values near the normalized minor radius of 0.5 to evaluate the quasilinear criterion. In experiments in TCV, the effects of radial diffusion reduce the observed ECCD by a factor 5 to 10. Also shown is the location where ITER will operate, assuming 20 MW of power at a minor radius of 0.5.

over the flux surface volume and n_{19} is the plasma density in units of 10^{19} m^{-3} . This criterion evaluated for TCV and for all the data points from DIII-D shown in Fig. 16 is shown in Fig. 20, using the ratio of the calculated ECCD to the measured ECCD as an indicator of quasilinear effects. In the TCV case the ratio of the quasilinear calculation neglecting transport to the linear calculation is used to characterize the importance of quasilinear effects, since transport is important in that device. The expected operating regime for ITER is also shown in this figure.

Figure 20 shows that the TCV experiments explore the interesting region of high power density where quasilinear effects should be strong. On the other hand, applications of EC power in ITER may be expected to be fully consistent with linear calculations. The experiments in DIII-D straddle the criterion, but exceed it at most by less than a factor of 2. Nevertheless, there is no systematic change in the behavior of the current drive when the criterion is approached, suggesting that the criterion may be conservative. This also indicates that the systematic increase in the measured ECCD efficiency relative to the efficiency calculated by the TORAY-GA code at the larger driven currents of Fig. 16(d) is not the result of quasilinear effects. Another experiment at high power density in which the quasilinear corrections are expected to be essential is the measurement of ECCD made on the Wendelstein VIIAS stellarator.⁹⁹ These experiments at power density up to $50 \text{ MW}/\text{m}^3$, an order of magnitude above the criterion, showed measured ECCD about a factor of 2 smaller than expected from linear calculations. Here quasilinear calculations showed that a strong non-Maxwellian component should be expected but quantitative agreement was not obtained. However, the discrepancy disappeared when the density was increased so that the quasilinear criterion was reduced by a factor of 6.

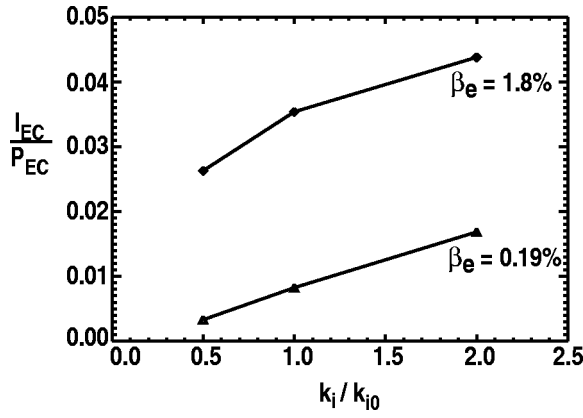


FIG. 21. Normalized value of ECCD calculated by TORAY-GA when the absorption coefficient k_i is arbitrarily modified by a factor from its calculated value k_{i0} , for a discharge from the DIII-D dataset with low β_e and for a comparison case with high β_e . The two cases correspond to the lowest and highest β_e cases of Fig. 5.

An interesting feature of the measurement of ECCD is that it provides a sensitive although indirect test of the absorption physics. The discussions in Sec. III C showed that the location of the resonance curve at the location of peak absorption rate has a strong effect on the net current drive, particularly if it lies near the trapping boundary in velocity space. This sensitivity can be quantified for any particular case. For example, for the DIII-D discharge with low β_e illustrated in Figs. 4, 5, and 12, the integrated absorbed power is calculated by the TORAY-GA code as greater than 99% of the incident power. If the absorption coefficient in TORAY-GA is arbitrarily increased or decreased by a factor of 2, then the absorbed power fraction is still greater than 99% while the calculated ECCD is changed by a factor greater than 2. This behavior is shown in Fig. 21. Since the low β_e discharge is one which appears in the data set of Fig. 16 as consistent with the experiment, it is clear that the absorption model in TORAY-GA is well validated experimentally to a much greater precision than could be determined directly from measurements of transmitted power.

IV. APPLICATIONS OF ECH/ECCD

The predictive model and quantitative understanding of the physics described in Secs. II and III can be used to optimize the application of ECH and ECCD for purposes of discharge improvement and analysis. The uniquely narrow heat and current drive profiles which can be generated by EC waves support some applications which cannot be addressed by other methods. This work has been discussed in a recent review,⁸ and here some recent progress is summarized.

A highlight of recent work with EC power has been the application of ECH or ECCD to stabilize or otherwise control MHD modes like sawteeth and neoclassical tearing modes as a means to improve discharge performance. This work takes full advantage of the very narrow deposition profiles possible with EC waves. The effect of EC power on sawteeth has been extensively studied on TCV^{75,76,106,107} and compared¹⁰⁸ with a detailed model using the PRETOR-ST code. This work showed that the sawtooth period could be

increased or decreased substantially with modest EC power, but highly accurate placement of the EC power (within ± 0.03 in ρ) is needed.⁷⁶ Similar results were found on TEXTOR.²³ An interesting outcome of these experiments is that the apparent width of the ECCD deposition appears to be even smaller than that calculated,¹⁰⁹ generating a challenge for systems in which a large number of beams is needed to sum to a high power or current density. The modification of sawtooth behavior has also been studied on the ASDEX Upgrade tokamak, partly as a means of removing the “seed island” in order to avoid destabilizing the neoclassical tearing mode (NTM).^{110–112} This work also reported use of ECCD in a systematic study of NTM onset conditions for comparison to theoretical models by varying the magnetic shear near the resonant surface. Experiments on JT-60U showed that early application of the ECCD, before the mode appeared, can keep the mode from ever appearing even at β above the threshold value without the ECCD.¹¹³

Several experiments in tokamaks have shown that very significant improvements in plasma performance can indeed accrue from stabilization of neoclassical tearing modes by localized ECCD. This work follows early experiments on stabilization of tearing modes by ECH^{114,115} which validated prior theoretic work¹¹⁶ and on stabilization of neoclassical tearing modes^{111,117} which also validated prior theory.^{118,119} Experiments on DIII-D showed that the onset of the mode with poloidal mode number $m=3$ and toroidal mode number $n=2$ caused the maximum supportable β to decrease by 25%, while adding ECCD to stabilize that mode allowed the β to be increased to 25% above the β of the initial onset.^{120,121} Similar results were reported from ASDEX Upgrade^{111,112} and JT-60U.¹²² Experiments on JT-60U showed that the $m=3/n=2$ NTM could be avoided completely by applying ECCD at the resonant surface before the mode appeared.¹¹³ This approach requires less EC power than stabilizing the mode after it has grown to a saturated amplitude. The more dangerous $m=2/n=1$ neoclassical tearing mode, which often leads to locked modes or disruptions, was stabilized consistently in DIII-D^{123–126} and ASDEX Upgrade.¹¹² The requirement that the ECCD align very accurately with the resonant surface for the magnetic islands in these experiments poses a challenge for control systems, since changes in the plasma equilibrium or the kinetic profiles can shift the location where the ECCD is needed. Automatic tracking systems are being developed on DIII-D, ASDEX Upgrade, and JT-60U to maintain the current drive at the needed location, even when the mode is absent. Active tracking has been used on DIII-D to maintain the β well above the onset value after the 3/2 NTM was stabilized without the instability restarting even in the presence of vigorous sawteeth and ELMs.¹²⁶ Taken as a whole, these results strongly support the use of ECCD in a burning plasma as a means of increasing plasma pressure to levels which would otherwise be unstable, thereby providing a major improvement in performance.

It should be noted that the ability of ECCD to fully stabilize neoclassical tearing modes indicates that the current driven by ECCD remains highly localized even in discharges with abundant MHD activity. In addition to the tearing mode

being acted on by the ECCD, these discharges have vigorous sawteeth and edge localized modes (ELMs), and in some cases other tearing modes and fishbone instabilities are present.^{127,117} Nevertheless, the calculated ECCD seems to fit well with the NTM theory. It is also striking that the calculations of ECCD which assume toroidal symmetry with averaging over a flux shell seem to work well for the case of helical islands. This issue is being addressed through application of a Fokker–Planck code¹²⁸ which is three dimensional in real space.

Modification and control of the current profile has demonstrated the potential to increase the confinement and stability properties in both tokamaks and stellarators, which is a key source of interest in EC waves.⁸ Experiments in DIII-D^{129–131} have shown that off-axis ECCD near $\rho=0.4$ in high performance plasmas with volume-averaged toroidal β around 3% can be sustained. The co-ECCD generates negative central magnetic shear, resulting in a weak transport barrier with resulting confinement improvement in the electron, ion, and particle transport channels even in ELMing H-mode plasmas. The noninductive current fraction reaches 90%. Work on JT-60U has shown the maintenance of an electron transport barrier in discharges with strong electron heating by a combination of ECH and a negative-ion-based neutral beam as a means of simulating the strong electron heating by alphas which will take place in a burning plasma.^{132,133} These discharges showed excellent global confinement with 55% of the power heating electrons and $T_e > T_i$. Experiments on the LHD stellarator, which has inherent negative shear, showed that when the central ECH power exceeds a threshold power at sufficiently low collisionality a strong electron transport barrier could form at normalized minor radius around 0.3 to 0.4, giving central electron temperatures above 10 keV and an overall increase in the global confinement time.^{134,135} The formation of the electron transport barrier is related to the strong radial electric field resulting from the neoclassical ambipolar flux in these high performance plasmas ($\beta \approx 3\%$).

Discharges with fully noninductive current have been achieved in the TCV tokamak.^{75,76} As described in Sec. III E the profile of ECCD is broad in TCV due to transport effects, but the well localized bootstrap current associated with the steep gradients of the transport barrier generate a reversed magnetic shear which in a positive feedback loop supports the transport barrier. Additional central ECH of 0.45 MW results in improved energy confinement by a factor of 2 compared with the scaling of the energy confinement with total power. Using counter-ECCD instead of ECH generates further increases in confinement, possibly because of increased negative shear. In these discharges the central safety factor is naturally larger than unity, so sawteeth are not present. The minor radius of the barrier is 0.3 to 0.4 and the bootstrap fraction is 80%. Far off-axis ECH has also been useful in TCV for increasing the conductivity near the plasma edge for broadening of the current profile, providing access to higher elongation operation.^{75,136} Modification of the safety factor profile by ECCD has also been seen on JT-60U.¹³⁷

One effect frequently associated with application of ECH power in toroidal confinement devices is the so-called

density pumpout effect.⁵ The phenomenology, first reported in the T-10 tokamak in 1976 (Ref. 138) but since observed in many tokamaks and the W7-AS stellarator, is that the application of ECH or ECCD may cause the density to redistribute radially, usually from the center toward the edge but sometimes the reverse, appearing as a decrease in the line-averaged density of 30% or more, or even for the total number of electrons in the plasma to decrease. However, in other cases little or nothing happens to the density profile. Several models have been developed to explain this phenomenon, but at present none has gained universal acceptance. One such model is that the particle confinement is related to the same turbulence which drives the ion thermal and momentum transport^{139,140} in high density H-mode plasmas in ASDEX Upgrade, and that this turbulence is sensitively related to the ratio T_e/T_i through stiff temperature profiles. This model has not yet been tested against the density behavior in other devices. A similar broadening affecting the “confinement zone” (that is, outside the $q=1$ surface) is also reported from TCV.¹⁴¹ A probably unrelated phenomenon is observed with central ECH when a quasicontinuous $m=1$ kink mode is present.¹⁴² In this case strong outward convection is observed inside the $q=1$ surface, leading to hollow density profiles. In the model proposed for this case,¹⁴³ the loss of toroidal symmetry inside the $q=1$ surface is at the origin of a reversal of the neoclassical thermodiffusive pinch.¹⁴⁴ Interestingly, the observation of peaked density profiles in MHD quiescent fully noninductive discharges (i.e., with zero toroidal electric field) in TCV demonstrates that inward pinch processes other than the Ware pinch must play a role.¹⁴² While it is disturbing that this pumpout phenomenon is not yet well understood some 30 years after it was first observed, that has not prevented the effect from being applied intentionally for the purpose of density control. For example, ECH is applied in experiments on ASDEX Upgrade with tungsten walls to suppress the accumulation of impurities in the plasma.¹⁴⁵ Similarly, ECH was applied in DIII-D on the quiescent double barrier mode of operation as an effective means of reducing the density peaking factor and the accumulation of high-Z impurities,¹³¹ resulting in a higher β limit, lower Z_{eff} , and reduced radiation losses.

The unique property of ECH which provides a very localized source of heating has been used in several devices to extensively probe the confinement properties of the plasma.^{5,8} Recent experiments on the FTU tokamak made use of a novel technique of applying modulated ECH out of phase in two nearby radial locations to modulate the local temperature gradient.¹⁴⁶ This method has been used to identify radial regions where the temperature gradient is close to a critical gradient so that the temperature profile is resistant to change.

ECH has been applied to discharges in the radiatively improved mode (RI-mode) in TEXTOR.²³ These experiments showed effective central heating up to central densities very nearly equal to the cutoff density for the applied 110 GHz X2-mode, which was attributed to minimal wave refraction due to a narrow beam pattern which was oriented radially. The RI-mode results also showed essentially no degradation in confinement when the ECH power was added,

in violation of the usual scaling laws. No degradation of confinement was also found even for a factor 5 increase in the electron heat flux when ECH was added inside a pre-existing transport barrier in ASDEX Upgrade.¹⁴⁷ In these discharges the ion transport and the angular momentum transport also did not deteriorate.

ECH was also applied to discharges with lower hybrid current drive in JT-60U¹⁴⁸ and Tore Supra.¹⁴⁹ In the JT-60U experiments central electron temperatures of order 25 keV were obtained with a flat profile out to the transport barrier at $\rho=0.4$, using 2.9 MW of ECH and 1.9 MW lower hybrid power. On Tore Supra, 1.8 MW of lower hybrid current drive (LHCD) power was used to develop a discharge with negative shear and minimum safety factor above unity to suppress the sawteeth. Then adding 0.3 MW of ECH near $\rho=0.2$ increases the electron temperature inside the transport barrier to 15 keV. Experiments on the FTU tokamak also showed formation of a durable transport barrier when LHCD is combined with ECH.^{150,151} These experiments were characterized by excellent global confinement and central electron temperatures up to 11 keV at the very high density of nearly 10^{21} m^{-3} . Finally, absorption of EC power on the fast electron tail has been observed in FTU under conditions of strong LHCD even when the cold electron cyclotron resonance does not lie in the plasma.¹⁵² The combination of LHCD and ECH appears to offer significant flexibility in controlling the heat and current profile.

V. SUMMARY

A new era has clearly arrived in which the beneficial attributes of ECH and ECCD are being exploited in laboratories around the world. The key features of EC waves—the ability to propagate in vacuum so that antennas far from the plasma edge can still couple power efficiently to the plasma, very high power density, robustly controllable heating location, and extremely narrow profile of deposited power or current—provide substantial motivation for applying EC waves to toroidal plasma confinement devices. The applications presently being pursued include plasma heating, modification and sustainment of desired profiles of plasma current, control or suppression of MHD activity like sawteeth and NTMs, and study of the transport properties of plasmas using the highly localized heating as a perturbation. The breadth and value of these activities has led to use of ECH in most magnetic confinement devices in operation today as well as inclusion in the plan for next step devices like Wendelstein 7X and ITER.

The application of EC waves to plasmas rests on a wide base of theoretical work which has been performed over the last 50 years or more. This work progressed from simple cold plasma models to hot plasma models with fully relativistic physics to quasilinear Fokker–Planck models to nonlinear computer simulations. It has been possible to test much of this theory in detail through development of computer codes for prediction and interpretation of experiments and comparison of the code results with experiment. Current drive by EC waves is quite sensitive to the magnitude of the wave absorption and the nature of the velocity-space inter-

action of the wave with electrons. Detailed comparisons with experiment show that theory is highly predictive over a wide range of parameters relevant to a reacting plasma. The projection of present results to future applications in burning plasma experiments can be done with confidence because the power densities will typically be lower than in present experiments, making nonlinear effects less likely to be important.

The availability of high power gyrotrons has supported the intensive use of ECH in many fusion-related experiments in recent years. Gyrotrons with diamond windows which can generate 1 MW of power in the frequency range 110 to 170 GHz with pulse length greater than 5 s have made experiments possible in modern large confinement devices where multi-megawatt systems are required. Because of the success of the physics and technology programs ECH is planned to fill critical roles in the next step devices.

ACKNOWLEDGMENTS

R.P. gratefully acknowledges valuable discussions or contributions from V.S. Chan, M. Choi, N.J. Fisch, T.P. Goodman, R.W. Harvey, A. Isayama, F. Leuterer, Y.-R. Lin-Liu, J. Lohr, T.C. Luce, C.C. Petty, R.I. Pinsker, A. Pochelon, P.A. Politzer, O. Sauter, and H. Zohm.

This work was supported by the U.S. Department of Energy under Contract No. DE-AC03-99ER54463.

¹M. Bornatici, R. Cano, O. De Barbieri, and F. Englemann, Nucl. Fusion **23**, 1159 (1983).

²R. Prater, in *Course and Workshop on Applications of RF Waves to Tokamak Plasmas*, edited by S. Bernabei, U. Gasparino, and E. Sindoni (International School of Plasma Physics, Perugia, 1985), Vol. I, p. 354.

³N. J. Fisch, Rev. Mod. Phys. **59**, 175 (1987).

⁴R. Prater, J. Fusion Energy **9**, 19 (1990).

⁵V. Erckmann and U. Gasparino, Plasma Phys. Controlled Fusion **36**, 1869 (1994).

⁶B. Lloyd, Plasma Phys. Controlled Fusion **40**, A119 (1998).

⁷N. A. Kirneva, Plasma Phys. Controlled Fusion **43**, A195 (2001).

⁸T. C. Luce, IEEE Trans. Plasma Sci. **30**, 734 (2002).

⁹ITER Physics Base Editors, Nucl. Fusion **39**, 2137 (1999).

¹⁰R. Prater, H. J. Grunloh, C. P. Moeller, J. L. Doane, R. A. Olstad, M. A. Makowski, and R. W. Harvey, in *Proceedings of the 10th Joint Workshop on Electron Cyclotron Emission and Electron Cyclotron Heating, Ameland, Netherlands, 1997*, edited by T. Donne and T. Verhoeven (World Scientific, Singapore, 1998), p. 531.

¹¹M. Thumm, Plasma Phys. Controlled Fusion **45**, A143 (2003).

¹²M. Thumm, Int. J. Infrared Millim. Waves **19**, 3 (1998).

¹³K. Sakamoto, A. Kasugai, M. Tsuneoka *et al.*, in *Proceedings of the 10th Joint Workshop on Electron Cyclotron Emission and Electron Cyclotron Heating, Ameland, Netherlands, 1997*, edited by T. Donne and T. Verhoeven (World Scientific, Singapore, 1998), p. 463.

¹⁴M. Thumm and W. Kasperek, IEEE Trans. Plasma Sci. **30**, 755 (2002).

¹⁵F. Leuterer, M. Beckmann, H. Brinkshulte *et al.*, Fusion Eng. Des. **53**, 485 (1999).

¹⁶A. W. Morris, P. G. Carolan, S. J. Fielding, C. Hunt, P. Leahy, B. Lloyd, and M. Valovic, in *Second Europhysics (Top. Conf. on Radio Frequency Heating and Current Drive of Fusion Devices)*, Vol. 22A, ECA, p. 213.

¹⁷J. Lohr, R. W. Callis, J. L. Doane, R. A. Ellis, Y. A. Gorelov, K. Kajiwara, D. Ponce, and R. Prater, *Proceedings of the 15th Topical Conference on Radio Frequency Power in Plasmas, Moran, Wyoming*, edited by C. B. Forest (AIP, New York, 2003), p. 335.

¹⁸S. Cirant, A. Bruschi, G. Granucci, A. Simonetto, G. Solari, P. Buratti, M. Santinelli, and O. Tudisco, in *Proceedings of the 9th Joint Workshop on Electron Cyclotron Emission and Electron Cyclotron Heating, Borrego Springs, California, 1995*, edited by J. Lohr (World Scientific, Singapore, 1995), p. 105.

- ¹⁹Y. Ikeda, A. Kasugai, K. Takahashi *et al.*, *Fusion Eng. Des.* **53**, 351 (2001).
- ²⁰Y. Ikeda, M. Seki, S. Moriyama *et al.*, in *Proceedings of the 12th Joint Workshop on Electron Cyclotron Emission and Electron Cyclotron Heating, Aix-en-Provence, France, 2002*, edited by G. Giruzzi (World Scientific, Singapore, 2002), p. 475.
- ²¹D. A. Kislov, *Proceedings of the 18th IAEA Fusion Energy Conference, Sorrento, Italy, 2000* (International Atomic Energy Agency, Vienna, 2000), Paper OV5/2 available online at <http://www.iaea.org/programmes/ripc/physics/fec2000/html/fec2000.htm>
- ²²M. Q. Tran, T. P. Goodman, M. Henderson *et al.*, in *Proceedings of the 10th Joint Workshop on Electron Cyclotron Emission and Electron Cyclotron Heating, Ameland, Netherlands, 1997*, edited by T. Donne and T. Verhoeven (World Scientific, Singapore, 1998), p. 305.
- ²³E. Westerhof, G. M. D. Hogewij, J. A. Hoekzema *et al.*, in *Proceedings of the 12th Joint Workshop on Electron Cyclotron Emission and Electron Cyclotron Heating, Aix-en-Provence, France, 2002*, edited by G. Giruzzi (World Scientific, Singapore, 2002), p. 395.
- ²⁴J. A. Hoekzema, W. A. Bongers, A. F. van der Grift *et al.*, in *Proceedings of the 12th Joint Workshop on Electron Cyclotron Emission and Electron Cyclotron Heating, Aix-en-Provence, France, 2002*, edited by G. Giruzzi (World Scientific, Singapore, 2002), p. 541.
- ²⁵C. Darbos, F. Bouquey, J. Clary *et al.*, in *Proceedings of the 12th Joint Workshop on Electron Cyclotron Emission and Electron Cyclotron Heating, Aix-en-Provence, France, 2002*, edited by G. Giruzzi (World Scientific, Singapore, 2002), p. 487.
- ²⁶S. Kubo, R. Kumazawa, T. Shimozuma *et al.*, in *Proceedings of the 13th Topical Conference on Radio Frequency Power in Plasmas, Annapolis, Maryland, 1999*, edited by S. Bernabei and F. Paoletti (AIP, New York, 1999), p. 237.
- ²⁷V. Erckmann, H. P. Laqua, H. Maaßberg, J. Geiger, G. Dammertz, W. Kasperek, and M. Thumm, *Fusion Eng. Des.* **53**, 365 (2001).
- ²⁸G. Michel, P. Brand, G. Dammertz *et al.*, in *Proceedings of the 12th Joint Workshop on Electron Cyclotron Emission and Electron Cyclotron Heating, Aix-en-Provence, France, 2002*, edited by G. Giruzzi (World Scientific, Singapore, 2002), p. 493.
- ²⁹K. Koppenburg, A. Arnold, E. Borie *et al.*, in *Proceedings of the 12th Joint Workshop on Electron Cyclotron Emission and Electron Cyclotron Heating, Aix-en-Provence, France, 2002*, edited by G. Giruzzi (World Scientific, Singapore, 2002), p. 433.
- ³⁰G. Bosia, in *Proceedings of the 12th Joint Workshop on Electron Cyclotron Emission and Electron Cyclotron Heating, Aix-en-Provence, France, 2002*, edited by G. Giruzzi (World Scientific, Singapore, 2002), p. 571.
- ³¹T. H. Stix, *Theory of Plasma Waves*, 2nd ed. (Wiley, New York, 1992), pp. 3–24.
- ³²C. P. Moeller, *Fusion Technol.* **15**, 725 (1989).
- ³³M. Greenwald, J. L. Terry, S. M. Wolfe, S. Ejima, M. G. Bell, S. M. Kaye, and G. H. Neilson, *Nucl. Fusion* **28**, 2199 (1988).
- ³⁴S. Alberti, T. P. Goodman, M. A. Henderson *et al.*, *Proceedings of the 18th IAEA Fusion Energy Conference, Sorrento, Italy, 2000* (International Atomic Energy Agency, Vienna, 2000), Paper PD/2 available online at <http://www.iaea.org/programmes/ripc/physics/fec2000/html/fec2000.htm>
- ³⁵S. Alberti, T. P. Goodman, M. A. Henderson, A. Manini, J.-M. Moret, P. Gomez, P. Blanchard, S. Coda, O. Sauter, and Y. Peysson, *Nucl. Fusion* **42**, 42 (2002).
- ³⁶J.-P. Hogge, S. Alberti, L. Porte, and G. Arnoux, in *Proceedings of the 12th Joint Workshop on Electron Cyclotron Emission and Electron Cyclotron Heating, Aix-en-Provence, France, 2002*, edited by G. Giruzzi (World Scientific, Singapore, 2002), p. 371.
- ³⁷A. K. Ram and A. Bers, in *Proceedings of the 12th Joint Workshop on Electron Cyclotron Emission and Electron Cyclotron Heating, Aix-en-Provence, France, 2002*, edited by G. Giruzzi (World Scientific, Singapore, 2002), p. 131.
- ³⁸J. Preinhardt and V. Kopecky, *J. Plasma Phys.* **10**, 1 (1973).
- ³⁹V. Erckmann, H. P. Laqua, H. Maaßberg, N. B. Maruschenko, M. Rome, F. Volpe, W. Kasperek, and G. A. Müller, *Proceedings of the 19th IAEA Fusion Energy Conference, Lyon, France 2002* (International Atomic Energy Agency, Vienna, 2002), Paper EX/W3, available online at <http://www.iaea.org/programmes/ripc/physics/fec2002/html/fec2002.htm>
- ⁴⁰V. Schevchenko, Y. Baranov, M. O'Brien, and A. Saveliev, in *Proceedings of the 12th Joint Workshop on Electron Cyclotron Emission and Electron Cyclotron Heating, Aix-en-Provence, France, 2002*, edited by G. Giruzzi (World Scientific, Singapore, 2002), p. 303.
- ⁴¹H. Laqua, in *Proceedings of the 15th Topical Conference on Radio Frequency Power in Plasmas, Moran, Wyoming*, edited by C. B. Forest (AIP, New York, 2003), p. 15.
- ⁴²R. Dumont and G. Giruzzi, *Phys. Plasmas* **6**, 660 (1999).
- ⁴³C. P. Moeller, V. S. Chan, R. J. La Haye, R. Prater, T. Yamamoto, A. Funahashi, K. Hoshino, and T. Yamauchi, *Phys. Fluids* **25**, 1211 (1982).
- ⁴⁴J. L. Doane, *Int. J. Infrared Millim. Waves* **13**, 1727 (1992).
- ⁴⁵S. E. Segre, *Plasma Phys. Controlled Fusion* **41**, 58 (1999).
- ⁴⁶H. Idei, S. Kubo, T. Shimozuma *et al.*, *Fusion Eng. Des.* **53**, 329 (2001).
- ⁴⁷H. Idei, S. Kudo, T. Shimozuma *et al.*, *Europhys. Conf. Abstr.* **24B**, 400 (2000).
- ⁴⁸S. Weinberg, *Phys. Rev.* **126**, 1899 (1962).
- ⁴⁹A. H. Kritz, H. Hsuan, R. C. Goldfinger, and D. B. Batchelor, *Proceedings of the 3rd International Symposium on Heating in Toroidal Plasmas, Grenoble, Italy, 1982* (ECE, Brussels, 1982), Vol. 2, p. 707.
- ⁵⁰K. Matsuda, *IEEE Trans. Plasma Sci.* **17**, 6 (1989).
- ⁵¹M. R. O'Brien, M. Cox, C. D. Warrick, and F. S. Zaitsev, *Proceedings of the IAEA Technical Committee Meeting on Advances in Simulation and Modeling of Thermonuclear Plasmas, Montreal, Canada, 1992* (IAEA, Vienna, 1993), p. 527.
- ⁵²E. Poli, G. V. Pereverzev, and A. G. Peeters, *Phys. Plasmas* **6**, 5 (1999); E. Poli, G. V. Pereverzev, A. G. Peeters, and M. Bornatici, *Fusion Eng. Des.* **53**, 9 (1999).
- ⁵³S. Cirant, S. Nowak, and A. Orefice, *J. Plasma Phys.* **53**, 345 (1995).
- ⁵⁴S. Nowak, E. Lazzaro, and G. Ramponi, *Phys. Plasmas* **3**, 4140 (1996).
- ⁵⁵R. W. Harvey, M. G. McCoy, and G. D. Kerbel, *Phys. Rev. Lett.* **62**, 426 (1989).
- ⁵⁶A. V. Timofeev, in *Reviews of Plasma Physics*, edited by B. B. Kadomtsev (Consultants Bureau, New York, 1989), Vol. 14, pp. 63–82.
- ⁵⁷I. Fidone, G. Granata, and R. L. Meyer, *Phys. Fluids* **25**, 2249 (1982).
- ⁵⁸E. Mazzucato, I. Fidone, and G. Granato, *Phys. Fluids* **30**, 3745 (1987); E. Mazzucato, I. Fidone, G. Giruzzi, and V. Krivenski, *Nucl. Fusion* **26**, 3 (1986).
- ⁵⁹H. Bindislev, in *Proceedings of the 9th Joint Workshop on Electron Cyclotron Emission and Electron Cyclotron Heating, Borrego Springs, California, 1995*, edited by J. Lohr (World Scientific, Singapore, 1995), p. 585.
- ⁶⁰G. Schmidt, *Physics of High Temperature Plasmas* (Academic, New York, 1966), p. 22.
- ⁶¹R. Prater, R. W. Harvey, Y. R. Lin-Liu, T. C. Luce, and C. C. Petty, in *Proceedings of the 14th Topical Conference on Radio Frequency Power in Plasmas, Oxnard, 2001*, edited by T. K. Mau and J. S. deGrassie (AIP, New York, 2001), p. 302.
- ⁶²R. Prater, C. C. Petty, R. Harvey, Y. R. Lin-Liu, J. Lohr, and T. C. Luce, *Europhys. Conf. Abstr.* **26B**, 4.057 (2002).
- ⁶³R. Prater, S. Ejima, R. W. Harvey *et al.*, *Proceedings of the 7th Topical Conference on Applications of Radio-Frequency Power to Plasmas, Kissimmee, Florida, 1987* (AIP, New York, 1987), p. 9; J.-Y. Hsu and C. P. Moeller, *ibid.*, p. 13.
- ⁶⁴K. K. Kirov, F. Leuterer, G. V. Pereverzev, F. Ryter, and W. Suttrop, *Plasma Phys. Controlled Fusion* **44**, 2583 (2002).
- ⁶⁵R. Prater, T. C. Luce, C. C. Petty *et al.*, *Europhys. Conf. Abstr.* **22C**, 3.080 (2002).
- ⁶⁶C. C. Petty, T. C. Luce, M. E. Austin, H. Ikezi, Y. R. Lin-Liu, J. Lohr, and R. Prater, in *Proceedings of the 13th Topical Conference on Radio Frequency Power in Plasmas, Annapolis, Maryland, 1999*, edited by S. Bernabei and F. Paoletti (AIP, New York, 1999), p. 245.
- ⁶⁷D. Akulina, G. Batanov, M. Berezetskii *et al.*, *Fusion Eng. Des.* **53**, 321 (2001).
- ⁶⁸F. Leuterer, K. Kirov, G. Pereverzev, F. Ryter, and D. Wagner, *Nucl. Fusion* **43**, 744 (2003).
- ⁶⁹J.-L. Segui, Y. Michelot, G. Giruzzi, T. P. Goodman, A. H. Kritz, A. Pochelon, O. Sauter, G. R. Smith, and M. Q. Tran, *Nucl. Fusion* **36**, 237 (1996).
- ⁷⁰S. L. Allen, M. D. Brown, J. A. Byers *et al.*, *Phys. Rev. Lett.* **72**, 1348 (1994).
- ⁷¹R. W. Harvey and R. Prater, in *Proceedings of the 14th Topical Conference on Radio Frequency Power in Plasmas, Oxnard, 2001*, edited by T. K. Mau and J. S. deGrassie (AIP, New York, 2001), p. 298.
- ⁷²A. Manini, J.-M. Moret, S. Alberti, T. P. Goodman, and M. A. Henderson, in *Proceedings of the 12th Joint Workshop on Electron Cyclotron Emission and Electron Cyclotron Heating, Aix-en-Provence, France, 2002*, edited by G. Giruzzi (World Scientific, Singapore, 2002), p. 365.
- ⁷³J.-M. Moret, S. M. Ahmed, S. Alberti *et al.*, *Plasma Phys. Controlled Fusion* **44**, B85 (2002).

- ⁷⁴S. Arnoux, S. Alberti, E. Nelson-Melby, L. Porte, and J. Ph. Hogge, CRPP Lausanne Report LRP768/03 (2003).
- ⁷⁵A. Pochelon, S. Alberti, G. Arnoux *et al.*, *Proceedings of the 15th Topical Conference on Radio Frequency Power in Plasmas*, Moran, Wyoming, edited by C. B. Forest (AIP, New York, 2003), p. 297.
- ⁷⁶M. A. Henderson, S. Alberti, C. Angioni *et al.*, *Phys. Plasmas* **10**, 1796 (2003).
- ⁷⁷S. Nowak, A. Airoidi, A. Bruschi, S. Cirant, F. Gandini, G. Granucci, E. Lazzaro, G. Ramponi, A. Simonetto, and C. Sozzi, *Fusion Eng. Des.* **53**, 315 (2001).
- ⁷⁸T. Ohkawa, "Steady state operation of tokamaks by rf heating," General Atomics Report GA-A13847 (1976); see National Technical Information Service Document PB2000-108008. Copies may be ordered from NTIS, Springfield, Virginia 22161.
- ⁷⁹N. J. Fisch and A. H. Boozer, *Phys. Rev. Lett.* **45**, 720 (1980).
- ⁸⁰V. S. Chan, S. C. Chiu, J. Y. Hsu, and S. K. Wong, *Nucl. Fusion* **22**, 787 (1982).
- ⁸¹J. Cordey, T. Edlington, and D. H. Start, *Plasma Phys.* **24**, 73 (1982).
- ⁸²R. H. Cohen, *Phys. Fluids* **30**, 2442 (1987).
- ⁸³Y. R. Lin-Liu, V. S. Chan, and R. Prater, *Phys. Plasmas* **10**, 4064 (2003).
- ⁸⁴T. C. Luce, Y. R. Lin-Liu, R. W. Harvey, G. Giruzzi, P. A. Politzer, B. W. Rice, J. Lohr, C. C. Petty, and R. Prater, *Phys. Rev. Lett.* **83**, 4550 (1999).
- ⁸⁵C. C. Petty, R. Prater, J. Lohr, T. C. Luce, W. R. Fox, R. W. Harvey, J. E. Kinsey, L. L. Lao, and M. A. Makowski, *Nucl. Fusion* **42**, 1366 (2002).
- ⁸⁶J. Decker, Y. Peysson, A. Bers, and A. K. Ram, in *Proceedings of the 12th Joint Workshop on Electron Cyclotron Emission and Electron Cyclotron Heating, Aix-en-Provence, France, 2002*, edited by G. Giruzzi (World Scientific, Singapore, 2002), p. 113.
- ⁸⁷C. F. Kennel and F. Englemann, *Phys. Fluids* **9**, 2377 (1966).
- ⁸⁸C. F. F. Karney, *Comput. Phys. Rep.* **4**, 183 (1986).
- ⁸⁹E. Westerhof, in *Proceedings of the 9th Joint Workshop on Electron Cyclotron Emission and Electron Cyclotron Heating, Borrego Springs, California, 1995*, edited by J. Lohr (World Scientific, Singapore, 1995), p. 3.
- ⁹⁰R. W. Harvey and M. G. McCoy, *Proceedings of the IAEA Technical Committee Meeting on Advances in Simulation and Modeling of Thermo-nuclear Plasmas, Montreal, Canada, 1992* (IAEA, Vienna, 1993), p. 498.
- ⁹¹G. Giruzzi, *Phys. Fluids* **31**, 3305 (1988); G. Giruzzi, I. Fidone, and X. Garbet, *Nucl. Fusion* **32**, 1011 (1992).
- ⁹²R. Prater, C. C. Petty, T. C. Luce *et al.*, in *Proceedings of the 15th Topical Conference on Radio Frequency Power in Plasmas, Moran, Wyoming*, edited by C. B. Forest (AIP, New York, 2003), p. 305.
- ⁹³O. Sauter, M. A. Henderson, F. Hofmann *et al.*, *Phys. Rev. Lett.* **84**, 3322 (2000).
- ⁹⁴O. Sauter, C. Angioni, S. Coda *et al.*, *Phys. Plasmas* **8**, 2199 (2001).
- ⁹⁵B. W. Rice, K. H. Burrell, L. L. Lao, and Y. R. Lin-Liu, *Phys. Rev. Lett.* **79**, 2694 (1997).
- ⁹⁶C. B. Forest, K. Kupfer, T. C. Luce, P. A. Politzer, L. L. Lao, M. R. Wade, D. G. Whyte, and D. Wroblewski, *Phys. Rev. Lett.* **73**, 2444 (1994).
- ⁹⁷L. L. Lao, J. S. deGrassie, Y. R. Lin-Liu, T. C. Luce, V. S. Chan, C. C. Petty, R. Prater, and H. E. St. John, in *Proceedings of the 14th Topical Conference on Radio Frequency Power in Plasmas, Oxnard, 2001*, edited by T. K. Mau and J. S. deGrassie (AIP, New York, 2001), p. 310.
- ⁹⁸C. C. Petty, Y. R. Lin-Liu, T. C. Luce, M. A. Makowski, R. Prater, D. I. Schuster, H. E. St. John, and K.-L. Wong, *Nucl. Fusion* **41**, 551 (2001).
- ⁹⁹J. Geiger, H. P. Laqua, H. Maaßberg, N. B. Marushchenko, C. Wendland, and M. Romé, *Proceedings of the 18th IAEA Fusion Energy Conference, Sorrento, Italy, 2000* (International Atomic Energy Agency, Vienna, 2000), Paper EXP4/04 available online at <http://www.iaea.org/programmes/ripc/physics/fec2000/html/fec2000.htm>
- ¹⁰⁰R. W. Harvey, O. Sauter, R. Prater, and P. Nikkola, *Phys. Rev. Lett.* **88**, 205001 (2002).
- ¹⁰¹R. C. Wolf, J. Hobirk, G. Conway *et al.*, *Proceedings of the 18th IAEA Fusion Energy Conference, Sorrento, Italy, 2000* (International Atomic Energy Agency, Vienna, 2000), Paper EX4/4 available online at <http://www.iaea.org/programmes/ripc/physics/fec2000/html/fec2000.htm>
- ¹⁰²T. Suzuki, S. Ide, T. Oikawa, Y. Ikeda, K. Kajiwarra, A. Isayama, T. Fujita, and K. Hamamatsu, *Plasma Phys. Controlled Fusion* **44**, 1 (2002).
- ¹⁰³T. Suzuki, S. Ide, K. Hamamatsu *et al.*, "Heating and current drive by electron cyclotron waves in JT-60U," to be published in *Nucl. Fusion*; Y. Takase and JT-60U Team, in *Proceedings of the 15th Topical Conference on Radio Frequency Power in Plasmas, Moran, Wyoming, 2003*, edited by C. B. Forest (AIP, New York, 2003), p. 235.
- ¹⁰⁴S. Coda, S. Alberti, P. Blanchard, T. P. Goodman, M. A. Henderson, P. Nikkola, Y. Peysson, and O. Sauter, *Nucl. Fusion* **43**, 1361 (2003).
- ¹⁰⁵C. C. Petty, R. Prater, T. C. Luce, R. A. Ellis, R. W. Harvey, J. E. Kinsey, L. L. Lao, J. Lohr, M. A. Makowski, and K.-L. Wong, *Nucl. Fusion* **43**, 700 (2003).
- ¹⁰⁶Z. A. Pietrzyk, C. Angioni, R. Behn *et al.*, *Phys. Plasmas* **7**, 2909 (2000).
- ¹⁰⁷Z. A. Pietrzyk, C. Angioni, R. Behn, S. Coda, T. P. Goodman, M. A. Henderson, F. Hofmann, and O. Sauter, *Phys. Rev. Lett.* **86**, 1530 (2001).
- ¹⁰⁸C. Angioni, T. P. Goodman, M. A. Henderson, and O. Sauter, *Nucl. Fusion* **43**, 455 (2003).
- ¹⁰⁹T. P. Goodman (private communication).
- ¹¹⁰T. P. Goodman, A. Mück, C. Angioni, M. A. Henderson, O. Sauter, F. Ryter, E. Westerhof, and H. Zohm, *Proceedings of the 19th IAEA Fusion Energy Conference, Lyon, France 2002* (International Atomic Energy Agency, Vienna, 2000), Paper EX/P5-11, available online at <http://www.iaea.org/programmes/ripc/physics/fec2002/html/fec2002.htm>
- ¹¹¹H. Zohm, C. Angioni, R. Arslanbekov *et al.*, *Proceedings of the 19th IAEA Fusion Energy Conference, Lyon, France 2002* (International Atomic Energy Agency, Vienna, 2000), Paper OV/2-1, available online at <http://www.iaea.org/programmes/ripc/physics/fec2002/html/fec2002.htm>
- ¹¹²S. Günter, G. Gantenbein, A. Gude, V. Igoshine, M. Maraschek, A. Mück, S. Saarelma, O. Sauter, A. C. C. Sips, and H. Zohm, *Nucl. Fusion* **43**, 161 (2003).
- ¹¹³K. Nagasaki, A. Isayama, and S. Ide, *Nucl. Fusion* **43**, L7 (2003).
- ¹¹⁴T-10 Group, *Proceedings of the 11th European Conference on Controlled Fusion and Plasma Physics, Aachen, Germany, 1983* (European Physical Society, Petit-Lany, Switzerland, 1983), Vol. 1, p. 289; V. V. Alikaev and V. Parail, in *Proceedings of the 4th International Symposium on Heating in Toroidal Plasmas, Roma, Italy*, edited by H. Knoepfel and E. Sindoni (International School of Plasma Physics, Varenna, 1984), Vol. II, p. 753.
- ¹¹⁵K. Hoshino, M. Mori, T. Yamamoto *et al.*, *Phys. Rev. Lett.* **69**, 2208 (1992).
- ¹¹⁶V. S. Chan and G. E. Guest, *Nucl. Fusion* **22**, 272 (1982).
- ¹¹⁷G. Gantenbein, H. Zohm, G. Giruzzi, S. Günter, F. Leuterer, M. Maraschek, J. Meskat, and Q. Yu, *Phys. Rev. Lett.* **85**, 1242 (2000).
- ¹¹⁸C. C. Hegna and J. D. Callen, *Phys. Plasmas* **4**, 2940 (1997).
- ¹¹⁹H. Zohm, *Phys. Plasmas* **4**, 3433 (1997).
- ¹²⁰R. Prater, R. J. La Haye, J. Lohr, T. C. Luce, C. C. Petty, J. R. Ferron, D. A. Humphreys, E. J. Strait, F. W. Perkins, and R. A. Ellis III, in *Proceedings of the 12th Joint Workshop on Electron Cyclotron Emission and Electron Cyclotron Heating, Aix-en-Provence, France, 2002*, edited by G. Giruzzi (World Scientific, Singapore, 2002), p. 239.
- ¹²¹R. Prater, R. J. La Haye, J. Lohr, T. C. Luce, C. C. Petty, J. R. Ferron, D. A. Humphreys, E. J. Strait, F. W. Perkins, and R. W. Harvey, *Nucl. Fusion* **43**, 1128 (2003).
- ¹²²A. Isayama, Y. Kamada, N. Hayashi *et al.*, *Proceedings of the 19th IAEA Fusion Energy Conference, Lyon, France, 2002* (International Atomic Energy Agency, Vienna, 2000), Paper EX/C2-2, available online at <http://www.iaea.org/programmes/ripc/physics/fec2002/html/fec2002.htm>
- ¹²³T. C. Luce, R. J. La Haye, D. A. Humphreys, C. C. Petty, R. Prater, M. E. Austin, D. P. Brennan, I. A. Gorelov, J. Lohr, F. W. Perkins, P. A. Politzer, and M. R. Wade, *Europhys. Conf. Abstr.* **26B**, 1.059 (2002).
- ¹²⁴C. C. Petty, R. J. La Haye, T. C. Luce, M. E. Austin, R. W. Harvey, D. A. Humphreys, J. Lohr, R. Prater, and M. R. Wade, in *Proceedings of the 15th Topical Conference on Radio Frequency Power in Plasmas, Moran, Wyoming*, edited by C. B. Forest (AIP, New York, 2003), p. 348.
- ¹²⁵C. C. Petty, R. J. La Haye, T. C. Luce *et al.*, *Nucl. Fusion* **44**, 243 (2004).
- ¹²⁶R. J. La Haye, D. A. Humphreys, J. Lohr, T. C. Luce, F. W. Perkins, C. C. Petty, R. Prater, and E. J. Strait, *Proceedings of the 19th IAEA Fusion Energy Conference, Lyon, France 2002* (International Atomic Energy Agency, Vienna, 2000), Paper EX/S1-3, available online at <http://www.iaea.org/programmes/ripc/physics/fec2002/html/fec2002.htm>
- ¹²⁷R. Prater, M. E. Austin, S. Bernabei *et al.*, *Proceedings of the 18th IAEA Fusion Energy Conference, Sorrento, Italy, 2000* (International Atomic Energy Agency, Vienna, 2000), Paper EX8/1 available online at <http://www.iaea.org/programmes/ripc/physics/fec2000/html/fec2000.htm>
- ¹²⁸P. R. da Silva Rosa and G. Giruzzi, *Plasma Phys. Controlled Fusion* **42**, 755 (2000).
- ¹²⁹M. Murakami, M. R. Wade, C. M. Greenfield *et al.*, *Phys. Rev. Lett.* **90**, 255001 (2003).
- ¹³⁰M. R. Wade, M. Murakami, T. C. Luce *et al.*, *Nucl. Fusion* **43**, 634 (2003).
- ¹³¹E. J. Doyle, T. A. Casper, K. H. Burrell *et al.*, *Proceedings of the 19th IAEA Fusion Energy Conference, Lyon, France, 2002* (International Atomic Energy Agency, Vienna, 2000), Paper EX/C3-2, available

- online at <http://www.iaea.org/programmes/ripc/physics/fec2002/html/fec2002.htm>
- ¹³²Y. Ikeda, S. Ide, A. Kasugai *et al.*, Nucl. Fusion **42**, 375 (2002).
- ¹³³S. Ide, T. Suzuki, Y. Sakamoto, H. Takenaga, T. Fujita, N. Oyama, A. Isayama, Y. Koide, and Y. Kamada, Nucl. Fusion **44**, 87 (2004).
- ¹³⁴K. Ida, T. Shimoizuma, H. Funaba *et al.*, Phys. Rev. Lett. **91**, 085003 (2003).
- ¹³⁵Y. Takeiri, T. Shimoizuma, S. Kubo *et al.*, Phys. Plasmas **10**, 1788 (2003).
- ¹³⁶A. Pochelon, G. Arnoux, Y. Camenen *et al.*, *Proceedings of the 19th IAEA Fusion Energy Conference, Lyon, France, 2002* (International Atomic Energy Agency, Vienna, 2000), Paper EX/P5-14, available online at <http://www.iaea.org/programmes/ripc/physics/fec2002/html/fec2002.htm>
- ¹³⁷T. Suzuki, S. Ide, C. C. Petty, Y. Ikeda, K. Kajiwara, A. Isayama, K. Hamamatsu, O. Naito, M. Seki, and S. Moriyama, *Proceedings of the 19th IAEA Fusion Energy Conference, Lyon, France, 2002* (International Atomic Energy Agency, Vienna, 2000), Paper EX/W-2, available online at <http://www.iaea.org/programmes/ripc/physics/fec2002/html/fec2002.htm>
- ¹³⁸V. V. Alikhaev, Fiz. Plasmy, **2**, 390 (1976) [Sov. J. Plasma Phys. **2**, 212 (1976)].
- ¹³⁹J. Stober, C. Fuchs, O. Gruber, M. Kaufmann, B. Kurzan, F. Meo, H. W. Müller, and F. Ryter, Nucl. Fusion **41**, 1535 (2001).
- ¹⁴⁰J. Stober, R. Dux, O. Gruber *et al.*, *Proceedings of the 19th IAEA Fusion Energy Conference, Lyon, France, 2002* (International Atomic Energy Agency, Vienna, 2000), Paper EX/C3-7Rb, available online at <http://www.iaea.org/programmes/ripc/physics/fec2002/html/fec2002.htm>
- ¹⁴¹A. Zabolotsky and H. Weisen, Plasma Phys. Controlled Fusion **45**, 735 (2003).
- ¹⁴²I. Furno, H. Weisen, and TCV Team, Phys. Plasmas **10**, 2422 (2003).
- ¹⁴³H. Weisen and I. Furno, Nucl. Fusion **41**, 1227 (2001).
- ¹⁴⁴L. M. Kovrizhnykh, Nucl. Fusion **24**, 851 (1984).
- ¹⁴⁵R. Neu, R. Dux, A. Geier *et al.*, Plasma Phys. Controlled Fusion **44**, 811 (2002).
- ¹⁴⁶S. Cirant, E. Lazzaro, and A. Bruschi, *Proceedings of the 19th IAEA Fusion Energy Conference, Lyon, France, 2002* (International Atomic Energy Agency, Vienna, 2000), Paper EX/C4-2Rb, available online at <http://www.iaea.org/programmes/ripc/physics/fec2002/html/fec2002.htm>
- ¹⁴⁷S. Günter, R. C. Wolf, F. Leuterer *et al.*, Phys. Rev. Lett. **84**, 3097 (2000).
- ¹⁴⁸S. Ide, T. Suzuki, Y. Sakamoto, H. Takenaga, Y. Koide, T. Fujita, T. Fukuda, Y. Kamada, H. Shirai, and T. Takizuka, Plasma Phys. Controlled Fusion **44**, A137 (2002).
- ¹⁴⁹F. Imbeaux, J. F. Artaud, V. Basiuk *et al.*, in *Proceedings of the 15th Topical Conference on Radio Frequency Power in Plasmas, Moran, Wyoming*, edited by C. B. Forest (AIP, New York, 2003), p. 275.
- ¹⁵⁰B. Angelini, M. L. Apicella, G. Apruzzese *et al.*, *Proceedings of the 19th IAEA Fusion Energy Conference, Lyon, France, 2002* (International Atomic Energy Agency, Vienna, 2000), Paper OV/4-5, available online at <http://www.iaea.org/programmes/ripc/physics/fec2002/html/fec2002.htm>
- ¹⁵¹V. Pericoli-Ridolfini, E. Barbato, P. Buratti *et al.*, *Proceedings of the 19th IAEA Fusion Energy Conference, Lyon, France, 2002* (International Atomic Energy Agency, Vienna, 2000), Paper EX/C3-6, available online at <http://www.iaea.org/programmes/ripc/physics/fec2002/html/fec2002.htm>
- ¹⁵²V. Pericoli-Ridolfini, Y. Peysson, R. Dumont, G. Giruzzi, G. Granucci, L. Panaccione, L. Delpech, and B. Tilia, *Proceedings of the 18th IAEA Fusion Energy Conference, Sorrento, Italy, 2000* (International Atomic Energy Agency, Vienna, 2000), Paper EX6/3, available online at <http://www.iaea.org/programmes/ripc/physics/fec2000/html/fec2000.htm>